

THE UNIVERSITY OF MANITOBA

OPTICAL TECHNIQUES FOR THE
DETERMINATION OF ELECTRIC FIELD
DISTRIBUTIONS
AND
FOR THE STUDY OF PREBREAKDOWN
PHENOMENA IN DIELECTRIC LIQUIDS

by

HACHIRO SUEDA

A Thesis

submitted to the Faculty of Graduate Studies
in partial fulfillment of the requirements for the
Degree of Doctor of Philosophy

Department of Electrical Engineering

Winnipeg, Manitoba

May 1980

OPTICAL TECHNIQUES FOR THE
DETERMINATION OF ELECTRIC FIELD
DISTRIBUTIONS
AND
FOR THE STUDY OF PREBREAKDOWN
PHENOMENA IN DIELECTRIC LIQUIDS

BY

HACHIRO SUEDA

A thesis submitted to the Faculty of Graduate Studies of
the University of Manitoba in partial fulfillment of the requirements
of the degree of

DOCTOR OF PHILOSOPHY

© 1980

Permission has been granted to the LIBRARY OF THE UNIVER-
SITY OF MANITOBA to lend or sell copies of this thesis, to
the NATIONAL LIBRARY OF CANADA to microfilm this
thesis and to lend or sell copies of the film, and UNIVERSITY
MICROFILMS to publish an abstract of this thesis.

The author reserves other publication rights, and neither the
thesis nor extensive extracts from it may be printed or other-
wise reproduced without the author's written permission.

A B S T R A C T

The work being presented in this thesis consists of three parts. The first part deals with the Schlieren images, observed in electrically stressed dielectric liquids. The second part deals with the new method for the determination of electric field distributions in dielectrics and along the interface between a dielectric liquid and a dielectric solid. The third part deals with the prebreakdown phenomena in high viscosity materials.

In the first part, experimental results for the Schlieren images observed in silicone oil are presented. The Schlieren images related to the liquid motion normally observed in electrically stressed dielectric liquids are discussed. The liquid motion is mainly caused by two mechanisms: (a) the Coulombic force due to the interaction of the space charge with the field, and (b) the electromechanical force created by the field resulting from the spatial variation of the dielectric constant due to the variation of temperature from domain to domain and from time to time in the liquid. The direction of such a liquid motion depends on which of these two mechanisms is dominant. The Schlieren images show mainly the change of the already-existing temperature gradients in the liquids, and this change is due to the liquid motion caused by either mechanisms (a) or (b) or both. It is concluded that the Schlieren images are directly governed by the temperature distribution in the liquid, and have no direct bearing on the formation and distribution of space charges.

In the second part, a new method for the determination of electric field distributions in dielectrics using a Schlieren optical system and

the applications are presented. This method is based on the principle that the spatial distribution of the refractive index produced by a small applied temperature difference is changed due to an electro-mechanical force created by the field resulting from the spatial variation of the dielectric constant. Some experimental results for benzene and n-hexane between two spherical electrodes obtained with this method show the essential features predicted from the space charge effects. This method has also been used for the measurements of the field distribution along the interface between a dielectric fluid and a dielectric solid. Some experimental results for the interfaces between n-hexane and a glass plate surface, and between n-hexane and a semiconducting layer surface obtained with this method, show that the space charge is the dominant factor controlling the field distributions. The other factors such as the dielectric constants and resistivities of the two materials forming the interface would play an important role in determining the field distributions if and only if the space charge effect is negligibly small or can be ignored. This method can be used to study electric field and space charge distributions along fluid-solid dielectric interfaces for practical insulation systems under both steady-state and transient conditions.

In the last part, experimental results for the effects of viscosity and applied field on the prebreakdown phenomena in high viscosity Epoxy are presented. The shadowgraphic image reflects only a region of disturbance occurring in a dielectric liquid, which differs in refractive index from its surroundings. The time required for the onset of a pre-

breakdown disturbance after the application of a step-voltage, and the rate of growth of the disturbance depend strongly on the viscosity (or the temperature) of the liquid. The refractive index inside the disturbance region is smaller than that outside it. The variation of the external current is consistent with the temporal change of the disturbance. It is proposed that the formation of a disturbance region is due to the Coulombic repulsion of local homocharges which in turn causes a decrease in local density and hence a decrease in refractive index. At high fields the anode injects holes to form positive ions and the cathode injects electrons, and the electric conduction is filamentary. The electric breakdown in condensed materials (liquids and solids) involves double injection and the creation of low density regions to enable the charge-carrier multiplication processes to take place. Thus the breakdown strength is governed by the parameters which control the conditions for such prebreakdown phenomena to arise.

ACKNOWLEDGEMENTS

The author wishes to express his deep appreciation to Professor K.C. Kao for suggesting the research topic and for his constant advice, supervision and encouragement throughout the entire work.

My sincere thanks are due to the researchers of Material Research Laboratory, and particularly to Drs. H. Adach and I. Kato and Messrs. Y. Kawai, L. Chow and G.A. Hjartarson for helpful discussions; to Messrs. S. Mejia and R.J. Sill for their technical assistance; to the staff of the Electrical Engineering of the University of Manitoba for their cooperation; and to Mrs. Paulette Giardino for typing this thesis.

Thanks are also due to the Natural Sciences and Engineering Research Council of Canada for supporting this project and to the Defense Agency of Japan for the grant of leave-of-absence.

T A B L E O F C O N T E N T S

<u>Chapter</u>		<u>Page</u>
1	INTRODUCTION	1
2	REVIEW OF PREVIOUS WORK	6
2.1	Optical Techniques for Studying Disturbances in Dielectric Liquids	6
2.1.1	The Kerr-Effect Method	7
2.1.2	The Doppler-Shift Method	12
2.2	Electric Field Distributions in Dielectric Systems	17
2.2.1	Electrical Field Distributions Between Parallel-Plane Electrodes	18
2.2.2	Electrical Field Distributions Along a Dielectric Solid	20
2.3	Disturbances in Electrically Stressed Dielectric Liquids	22
2.3.1	Electrohydrodynamic Motion	22
2.3.2	Prebreakdown Phenomena	25
2.4	Breakdown Processes	35
3	THE OPTICAL MEASURING SYSTEM	42
3.1	The Schlieren Optical Method	42
3.1.1	The Basic Principle of the Schlieren Optical Method	43
3.1.2	The Schlieren Optical System used for Measurements of Field Distributions and Other Disturbances	48
3.1.3	The Measurements of Temperature Gradients	55

<u>Chapter</u>	<u>Page</u>
3.2 The Shadowgraphic Method	61
3.2.1 The Basic Difference Between the Shadowgraphic Method and the Schlieren Method	61
3.2.2 The Shadowgraphic System used for the Studies of Prebreakdown Phenomena	64
4 THE SCHLIEREN IMAGES	66
4.1 Theory	66
4.2 Experimental Techniques	70
4.3 Experimental Results and Discussion	72
5 SCHLIEREN METHOD FOR THE DETERMINATION OF ELECTRIC FIELD DISTRIBUTIONS IN DIELECTRICS	91
5.1 Theory	92
I FIELD DISTRIBUTIONS BETWEEN SPHERE-SPHERE ELECTRODES	99
5.2 Experimental Techniques	99
5.3 Experimental Results and Discussion	101
II ELECTRIC FIELD DISTRIBUTIONS ALONG FLUID-SOLID DIELECTRIC INTERFACES	112
5.4 Experimental Techniques	113
5.5 Experimental Results and Discussion	116
6 PREBREAKDOWN PHENOMENA IN HIGH VISCOSITY DIELECTRIC LIQUIDS	134
6.1 Experimental Techniques	135
6.2 Experimental Results and Discussion	140
7 CONCLUSIONS	152
REFERENCES	153

LIST OF TABLES

<u>Table</u>		<u>Page</u>
2.1	The Kerr's constant K_k and the characteristic electric field E_{k0} of some dielectric liquids	13
2.2	Pressure dependence of corona inception voltage in the dielectric oil	32
2.3	Comparison of the breakdown theory with experiment . . .	41
4.1	The summary of the results about the relative maximum change in δ_y and the time t required for such a change to reach a peak value under various conditions	83

LIST OF FIGURES

<u>Figure</u>	<u>Page</u>
2.1 The basic optical system based on the Kerr-effect. L.S: ligh source; L.E: light expander; Po: Polarizer; Co: Compensator; F: Focusing lens; A _n : Analyzer; S: screen.	8
2.2 A typical fringe pattern in nitrobenzene photographed (exposure time 0.3 μ s) at the peak of a 65.4 kV total- duration 10 μ s pulse. The fact that the field is uniform between the plates is demonstrated by the absence of interelectrode fringe. The side fringes are due to the fringing field along the length of the electrodes . . .	11
2.3 The Doppler shift method. v_w : velocity of a wave in medium; v_m : velocity of a medium; L_b : laser beam; v_d : velocity of an observer; V_s : velocity of a wave source; mi: mirror; sp: splitter; Fi: filter.	14
2.4 Electric field distortions introduced in a uniform field gap in nitrobenzene by various dielectric spacers bridging the gap	21
2.5(a) The photographs of propagation of prebreakdown disturbances produced by the impulse breakdown between point-plane electrodes in dielectric oil. These pictures were taken by Schlieren method, using a xenon flash lamp and a Beckman camera Applied voltage: 36 kV, 1 x 140 μ s, frame separation: 66.5 μ s, exposure time: 3.6 μ s; pressure: 0.5 mm Hg, gap length: 25.4 mm	26
2.5(b) The photographs of propagation of prebreakdown disturbances produced by the impulse breakdown between point-point electrodes in liquid notrogen. These pictures were taken by Schlieren method using a ring edge temperature -196°C, pressure 1 atm, gap length 6 mm, applied impulse voltage 58 V	27
2.6 Velocities of prebreakdown disturbances in white oil . . .	29
2.7 The effects of pressure on the streamer propagation . . .	32
2.8 The effects of additives on the propagation rates	33
2.9 The dependence of breakdown strength of some organic liquids upon applied hydrostatic pressure	37

<u>Figure</u>	<u>Page</u>
3.1 The basic Schlieren system. L.S: light source; C ₁ : condenser lens; H: pin-hole; C ₂ collimating lens; S: slit to control the size of the light beam entering the test region; F: Schlieren lens; F _S : Focal length of lens F	44
3.2 The Schlieren system. L.S: He-Ne laser (light source); D, diffusing lens; C, collimating lens; S, slit to control the size of the light beam entering the test region; F, Schlieren lens; M, magnifying lens	49
3.3 Typical variation of the image brightness on the screen with the knife edge position along the v-direction (with respect to an arbitrary reference position)	51
3.4 The detectable refracted angle ϕ_d as a function of the diameter of the parallel beam. A: $f_s = 200$ mm; B: $f_s = 500$ mm	53
3.5 Typical variation of the image brightness on the screen for the light passing through near the solid surface with the knife edge position along the y-direction (with respect to an arbitrary reference position)	54
3.6 δ_y as a function of temperature difference $T_1 - T_2$ for (A) benzene and (B) n-hexane (with respect to an arbitrary reference position)	58
3.7 Shadowgraphic system. L.S: light source; C ₁ : condenser lens; H: pin-hole; C ₂ : collimating lens; F: focusing lens; M: magnifying lens	62
3.8 Electro-optical system for the observation of prebreak-down phenomena. D: diffusing lens; C: collimating lens; F: focusing lens; M: magnifying lens	65
4.1 The electrode system for the study of the Schlieren images in electrically stressed dielectric liquids. A, stainless steel blade; B, 0.2 mm thick copper plate; C, Teflon electrode supporting frame; P ₁ and P ₂ , measuring points of temperature gradients	71

<u>Figure</u>	<u>Page</u>
<p>4.2 Illustrating the change of the original temperature gradient at $t = 0$, $(dT/dy)_0$, resulting from the liquid motion caused predominantly by the motion of ions. (A) $(dT/dy)_0 > 0$ at $t = 0$; $(dT/dy)_1 > \theta_1 > \theta_0$; and $(dT/dy)_2$, $\theta_2 < \theta_0$; electromechanical force in the direction opposite to the ionic motion. (B) $(dT/dy)_0 < 0$ at $t = 0$; $(dT/dy)_1 < (dT/dy)_0$, $(2\pi - \theta'_1) < (2\pi - \theta'_0)$; and $(dT/dy)_2 < (dT/dy)_0$, $(2\pi - \theta'_2) < (2\pi - \theta'_0)$; electromechanical force in the same direction as the ionic motion</p>	74
<p>4.3 Schlieren photographs for silicone oil after the application of + 7 kV to the blade at $t = 0$ showing the effect of the already-existing temperature gradient in the test region. (A) $(dT/dy)_0 > 0$ corresponding to the knife edge setting of $5\mu\text{m}$; a, $t = 0.5$ sec; b, $t = 1.0$ sec; c, $t = 8.0$ sec; (B) $(dT/dy)_0 < 0$ corresponding to the knife edge setting of $30\mu\text{m}$</p>	76
<p>4.4 The temperature gradient in terms of δ_y measured at point P_1 (0.7 mm above the plate) after the application of + 7 kV to the blade as a function of the initial temperature gradient $(dT/dy)_0$ in terms of setting of the knife edge at zero applied voltage</p>	79
<p>4.5 The temperature gradient in terms of δ_y measured at point P_1 (0.7 mm above the plate) after the application of - 7 kV to the blade as a function of the initial temperature gradient $(dT/dy)_0$ in terms of setting of the knife edge at zero applied voltage</p>	80
<p>4.6 The variation of δ_y with time measured at point P_1 (0.7 mm above the plate) after the application of 7 kV to the blade at $t = 0$ (witch on) and after the removal of the applied voltage at t of about 20 sec (switch off). (a) Applied voltage: + 7 kV; A: $(dT/dy)_0 > 0$ corresponding to the knife edge setting of $13.4\mu\text{m}$; B: $(dT/dy)_0 < 0$ corresponding to the knife edge setting of $25.5\mu\text{m}$; (b) Applied voltage: - 7 kV; A: $(dT/dy)_0 > 0$ corresponding to the knife edge setting of $10\mu\text{m}$; B: $(dT/dy)_0 < 0$ corresponding to the knife edge setting of $30\mu\text{m}$</p>	82

<u>Figure</u>	<u>Page</u>
4.7 The variation of δ_y with time measured at point P_1 (0.7 mm above the plate) and point P_2 (0.9 mm below the plate) after the application of ∓ 7 kV to the blade at $t = 0$. (A) $(dT/dy)_0 > 0$ corresponding to the knife edge setting of $6\mu\text{m}$; (B) $(dT/dy)_0 < 0$ corresponding to the knife edge setting of $31\mu\text{m}$. . .	85
4.8 The variation of δ_y with time measured at point P_1 (0.7 mm above the plate) and point P_2 (0.9 mm below the plate) after the application of -7 kV to the blade at $t = 0$. (A) $(dT/dy)_0 > 0$ corresponding to the knife edge setting of $3\mu\text{m}$; (B) $(dT/dy)_0 < 0$ corresponding to the knife edge setting of $25\mu\text{m}$	86
4.9 Current I and the percent change in δ_y (measured at a point 0.2 mm below the blade edge) as functions of voltage V applied to the blade for $(dT/dy)_0 >$ corresponding to the knife edge setting of $-2362\mu\text{m}$.	88
4.10 The variation of δ_y with the distance from the plate surface along the y direction. $\delta_y = 1$ unit corresponding to a relatively constant temperature gradient at the plate surface is used as the reference	90
5.1 (A) The electrode system. A and B - parallel copper plates, C - four glass tubes, D - two spherical electrodes. (B) The mesh diagram showing the positions of the points for electric field distribution measurements in the test region	100
5.2 Schlieren photographs for benzene showing the effect of applied voltages between two spherical electrodes on the temperature distribution in the test region .	103
5.3 Schlieren photographs for n-hexane showing the effect of applied voltages between two spherical electrodes on the temperature distribution in the test region .	104
5.4 The ratio \bar{A}/\bar{B} as a function of the square of the applied voltage for benzene. Dashed curves for the points near the negative electrode and solid curves for the points near the positive electrode. a: $x = 5, y = 10$; b: $x = 10, y = 10$; c: $x = 5, y = 6$; d: $x = 10, y = 6$; e: $x = 5, y = 4$; f: $x = 10, y = 4$.	106

<u>Figure</u>		<u>Page</u>
5.5	The ratio \bar{A}/\bar{B} as a function of the square of the applied voltage for n-hexane. Dashed curves for the points near the negative electrode and solid curves for the points near the positive electrode. a: x = 10.1, y = 10; b: x = 4.6, y = 10; c: x = 10.1, y = 6; d: x = 4.6, y = 6; e: x = 10.1, y = 4; f: x = x = 4.6, y = 4	107
5.6	The ratio \bar{A}/\bar{B} as a function of y at various applied voltages for benzene. Dashed curves for the points near the negative electrode at a fixed x = 5 and solid curves for the points near the positive electrode at a fixed x = 10. a and b: 20 kV; c and d: 18 kV; e and f: 16 kV; g and h: 14 kV; j: 12 kV; k: 10 kV . . .	109
5.7	The ratio \bar{A}/\bar{B} as a function of y at various applied voltages for n-hexane. Dashed curves for the points near the negative electrode at a fixed x = 4.6 and solid curves for the points near the positive electrode at a fixed x = 10.1. a and b: 20 kV; c and d: 16 kV; e and f: 12 kV; g and h: 8 kV . . .	110
5.8	The percent change in the ratio \bar{A}/\bar{B} as a function of x along the central line connecting the electrode centers at y = 10. Applied voltage: 16 kV. The values of \bar{A}/\bar{B} marked with arrows are used as references	111
5.9	Electrode system for measurement of electric field distributions along the liquid-solid dielectric interfaces. A, to high voltage source; B, to electrometer; C, teflon framework; D, glass plates; E, metallic rod contact; T, top aluminum electrode; H, aluminum block (bottom electrode)	114
5.10	Schlieren image photographs without applied fields. (A) initial temperature gradient $(dT/dy)_0 = 0$; (B) $(dT/dy)_0 = 0.7^\circ\text{C}/\text{cm}$	117
5.11	Schlieren image photographs with applied voltages. (A) V = + 5 kV, $(dT/dy)_0 = 0.7^\circ\text{C}/\text{cm}$; (B) V = - 5 kV, $(dT/dy)_0 = 0.7^\circ\text{C}/\text{cm}$; (C) V = + 10 kV, $(dT/dy)_0 = 0.7^\circ\text{C}/\text{cm}$; (D) V = - 10 kV, $(dT/dy)_0 = 0.7^\circ\text{C}/\text{cm}$	119

<u>Figure</u>	<u>Page</u>
5.12 Electric field distribution along the interface between n-hexane and a glass plate for negative (O) and positive (O) dc voltages applied to the top electrode. (A) - 2 kV, (B) + 2 kV, (C) - 4 kV, (D) + 4 kV, (E) - 6 kV, (F) + 7 kV, (G) - 8 kV, (H) + 8 kV .	121
5.13 Electric field distribution along the interface between n-hexane and a glass plate for 60 Hz ac voltages applied to the top electrode (A) 2 kV, (B) 4 kV, (C) 6 kV, (D) 7 kV	123
5.14 Electric field distribution along the interface between n-hexane and a glass plate for a specially cleaned glass plate surface. (A) 2 kV ac, (B) 4 kV ac, (E) 8 kV ac, (G) - 8 kV dc, (H) + 8 kV dc	125
5.15 The current through the interface between n-hexane and a $\text{Se}_{0.78}\text{Te}_{0.22}$ semiconductor film as a function of applied voltage. 0 - dc voltages, 0 + dc voltages. (A) Light intensity: 35 mW/cm ² , (B) 385 mW/cm ² , (C) 1660 mW/cm ²	127
5.16 Electric field distribution along the interface between n-hexane and a $\text{Se}_{0.78}\text{Te}_{0.22}$ semiconductor film for negative (O) and positive (O) dc voltages applied to the top electrode and under illumination with the light intensity of 385 mW/cm ² . (A) 4 kV, (B) 8 kV, (C) 10 kV, (D) 12 kV	128
5.17 Electric field distribution along the interface between n-hexane and a $\text{Se}_{0.78}\text{Te}_{0.22}$ semiconductor film for positive dc voltages applied to the top electrode and under illumination with the light intensity of 385 mW/cm ² . (A) 4 kV, (B) 8 kV, (C) 10 kV, (D) 12 kV.	130
5.18 Electric field distribution along the interface between n-hexane and a $\text{Se}_{0.78}\text{Te}_{0.22}$ semiconductor film for negative dc voltages applied to the top electrode and under illumination with the light intensity of 385 mW/cm ² . (A) - 4 kV, (B) - 8 kV, (C) - 10 kV, (D) - 12 kV	131

<u>Figure</u>	<u>Page</u>	
5.19	The peak electric field along the interface between n-hexane and a $\text{Se}_{0.78}\text{Te}_{0.22}$ semiconductor film as a function of voltage applied to the top electrode at various light intensities. (A) light intensity of 35 mW/cm^2 , positive dc voltage; (B) light intensity of 35 mW/cm^2 , negative dc voltages; (C) light intensity of 1660 mW/cm^2 , positive dc voltages; (D) light intensity of 1660 mW/cm^2 , negative dc voltages	133
6.1	The point-point electrode system for the observation of prebreakdown phenomena. A, copper plate connected to neutral ground; B, point-point electrode holder	136
6.2	Experimental arrangement for the measurement of the change of the refractive index in the disturbance reion	139
6.3	The photographs of the disturbances produced by the applied voltage of 48 kV between point-point electrodes with a gap length of 0.3 cm in epoxy fluid at temperature of -5.5°C	141
6.4	The photographs of the disturbances produced by the applied voltage of 34 kV between point-point electrodes with a gap length of 0.3 cm in epoxy fluid at temperature of $+5.6^\circ\text{C}$	142
6.5	The viscosity (A), the time required for the first appearance of the disturbance after the application of a step voltage of 48 kV (B), and the speed of the growth of the disturbance at the applied voltage of 48 kV (C) in epoxy fluid. Electrodes, point-point; gap length, 0.3 cm	143
6.6	Number of bursts of carriers injected from the point electrode per second as a function of temperature for epoxy fluid with a point-point electrode configuration of gap length of 0.3 cm. A, $f_p = 2.15 \times 10^6 \text{ V cm}^{-1}$ (negative point); B, $E_p = 2.15 \times 10^6 \text{ V cm}^{-1}$ (positive point); C, $E_p = 1.70 \times 10^6 \text{ V cm}^{-1}$ (negative point); D, $E_p = 1.70 \times 10^6 \text{ V cm}^{-1}$ (positive point)	146

<u>Figure</u>	<u>Page</u>
6.7 Average current as a function of temperature for epoxy fluid with a point-plane electrode configuration of gap length of 0.3 cm. A, $E_p = 2.15 \times 10^6 \text{ V cm}^{-1}$ (negative point); B, $E_p = 2.15 \times 10^6 \text{ V cm}^{-1}$ (positive point); C, $E_p = 1.70 \times 10^6 \text{ V cm}^{-1}$ (negative point); D, $E_p = 1.70 \times 10^6 \text{ V cm}^{-1}$ (positive point)	147
6.8 The reflected light intensity as a function of angle of incidence of light incident on the surface of the disturbance region	149

LIST OF MOST USED SYMBOLS

E	Electric field
E_b	Breakdown field strength
E_k	Electric field for transmitted light minima in a Kerr-effect system
E_{k0}	Characteristic electric field of a Kerr cell
F	Force for electrohydrodynamic motion
f	Electromechanical force
f_s	Focal length of the lens
g	Gravitational acceleration
I	Current
K_k	Kerr's constant
K_n	Temperature coefficient of the refractive index of the medium
K_ϵ	Temperature coefficient of the dielectric constant of the medium
K_ρ	Temperature coefficient of the density of the medium
N	Density of ions
n	Refractive index
n_a	Refractive index of the medium outside a test region
n_o	Average refractive index of the medium
q	Electron charge
R	Radius of the lens
T	Temperature
T_o	Average temperature
T_R	Temperature at a reference point

δ	Deflecting distance
δ_x	Deflecting distance for x-direction
δ_y	Deflecting distance for y-direction
ϵ	Dielectric constant
ϵ_0	Dielectric constant of the medium corresponding to the average temperature of the system
θ	Refracted angle inside the test region
θ_x	Refracted angle in the x-z plane
θ_y	Refracted angle in the y-z plane
λ	Wavelength of the light
ρ	Density of the medium
ρ_0	Density of the medium corresponding to the average temperature of the system
ϕ	Refracted angle outside the test region
ϕ_d	Detectable refracted angle

CHAPTER 1

INTRODUCTION

High-field electric conduction and breakdown phenomena in dielectric liquids have been extensively studied by many investigators for more than fifty years. However, from both the experimental results and the many theoretical approaches published in the literature, it is shown that there is no one unified theory which can explain beyond doubt all the experimental results. The slow progress of this field can be considered as due at least partly to the discrepancy among the experimental results reported by different investigators which may be mainly caused by different experimental conditions used by them. Thus, in the past two decades, investigators have given much attention to sample purity and electrode preparation, and have improved techniques to control their experimental conditions in order to obtain reproducible results. They have also developed new experimental techniques to study the prebreakdown phenomena from different angles. These efforts have shed some light upon the understanding of this field. Prior to breakdown, there are always some disturbances created by high electric fields. Such disturbances have been studied by means of Schlieren, shadowgraphic, Kerr-effect and other optical methods, such as disturbances related to electrohydrodynamic motion [Gray and Lewis 1969, Hewish and Bringmell 1975, Usuda and Sakamoto 1977], to particle migration [Poulter and Snaddon 1978], to electrostriction [Hakim and Higham 1962] to electric field distribution

[Cherney and Cross 1973, Cassidy et al. 1974] and to prebreakdown and breakdown phenomena [Farazmand 1961, Morikawa 1972, Heiman et al. 1976, Chiu 1976].

Since an optical image of a phenomenon shows only a region which has a different refractive index, it, in general, does not provide any information about the mechanisms responsible for its occurrence, though the conditions for its occurrence may be known. We have had to search for the mechanisms from the relations between the images and other experimental results. The difficulty is mainly due to the lack of other data to help the analysis of the optical observations. Therefore, to study any disturbance it is important to observe the phenomenon optically and to measure simultaneously the other properties which are related to this phenomenon.

The Schlieren optical method can detect only the difference in refractive index in a domain of interest. If this method is employed for studying the physical processes responsible for any disturbance in an electrically stressed dielectric liquid, the first question to be asked is: what are the factors resulting in a change of the refractive index? The answer to this question not only would give some hints to the mechanisms responsible for the occurrence of a disturbance, but also would lead to further development of this method. Therefore, at first, we have to clarify the interpretation of the Schlieren images normally observed in electrically stressed dielectric liquids.

For studying the charge transport and breakdown processes in dielectrics, the measurements of field distributions are extremely

important. Up to now the field distributions, in general, are measured by means of a probe or the Kerr-effect. However, the probe may disturb the potential distributions and the Kerr-effect can be applied only to those materials, the anisotropy of whose refractive index is field dependent. In fact the Kerr-effect can be observed significantly only for a few materials such as nitrobenzene and chlorobiphenyls. We have therefore developed a new technique for the determination of field distributions. This technique is non-destructive and non-disturbing, and it can be applied to any dielectric systems. We have used this method for studying the field distributions in liquid and along the liquid-solid interfaces.

Electric breakdown is generally preceded by the growth of a disturbance whose refractive index is different from that of its surroundings [Sharbaugh et al. 1978]. In the past, the study of such a pre-breakdown disturbance has been concentrated on low viscosity dielectric liquids or almost infinite viscosity dielectric solids with applied fields very close to their breakdown strength. However, the information so far gathered has not been sufficient to indicate with certainty the origins and the nature of prebreakdown disturbances. One of the difficulties of the studies of the prebreakdown phenomena is that the propagation velocity of the disturbances in low viscosity dielectric liquids is very fast and it is necessary to have a high speed camera or recording system to record them. Recently, several investigators have developed an ultra-high speed electro-optical system with a time resolution of the order of 10^{-8} sec, and they have observed the pre-

breakdown phenomena in n-hexane just a few nsec prior to breakdown [Forster and Wong 1977, Rzad et al. 1977]. All of this kind of observations can provide only the information about the change of the refractive index in the disturbance regions. To explore the mechanisms responsible for the appearance of such disturbances, several investigators have measured the electrical and optical properties and recorded the disturbances simultaneously in order to correlate them under various conditions [Morikawa 1972, Chiu 1976, Heiman et al. 1976, Yamashita et al. 1977, Murooka and Sueda 1976, Forster and Wong 1977].

While a great deal of work has been concentrated on low viscosity liquids, we have attempted to study such prebreakdown phenomena from a different angle. We chose a material with viscosity sufficiently high and sensitive to temperature, so that we could use a conventional movie camera in conjunction with a simple shadowgraphic system to study the effects of viscosity and applied field on the prebreakdown phenomena. The high viscosity is usually accompanied with a slow development of prebreakdown disturbances, and this would therefore help to observe the details of the temporal change of the disturbances. Furthermore, the high-viscosity materials lie in the state between the liquid of low viscosity and the solid of almost infinite viscosity [Krasucki 1966], thus, a study of these high-viscosity materials may not only throw light on the understanding of the breakdown mechanisms in liquid dielectrics but also to the prebreakdown disturbance generally referred to as treeing in solids.

Before presenting our theory and results, it is desirable to

review briefly the most important work relevant to this thesis in order to give a clear view in this field. Thus, Chapter 2 will be devoted to this review. Chapter 3 will describe the optical techniques used in this investigation. The major work on the theory of the Schlieren images in electrically stressed dielectric liquids is presented in Chapter 4. A new method for the determination of electric field distributions and other applications is presented in Chapter 5. Pre-breakdown phenomena in high viscosity material are discussed in Chapter 6. The general conclusions arising from the present work are given in Chapter 7.

CHAPTER 2

REVIEW OF PREVIOUS WORK

In this chapter, a brief review of the previous work on optical techniques, electric field distributions, electrohydrodynamic motion, and prebreakdown and breakdown phenomena in dielectric liquids is presented. Although the investigators in this field, in general, have an interest in mechanisms responsible for these phenomena; the experimental results, on the basis of which a theory is developed, depend at least partly on the experimental techniques used. Thus, the techniques for detecting disturbances are reviewed first, and then followed with the electric field distribution, and prebreakdown and breakdown phenomena related to the work being presented in this thesis.

2.1 Optical-Techniques for Studying Disturbances in Dielectric Liquids

There are several optical methods which can be used for studying the disturbances in dielectric liquids. However, the most important ones are the Schlieren optical method, shadowgraphic method, the Doppler-shift method and the Kerr-effect method. Many investigators have used these methods for studying the prebreakdown and breakdown phenomena, and other disturbances in dielectrics. Although their principles and applications are well known, these methods have not yet been fully discussed from the view point of practical problems involved. The Schlieren optical method and shadowgraphic method will be discussed in Chapter 3, because they are used for our investigation. Therefore in this section, we shall confine ourselves to the discussion of only the Kerr-effect and the Doppler-shift

methods.

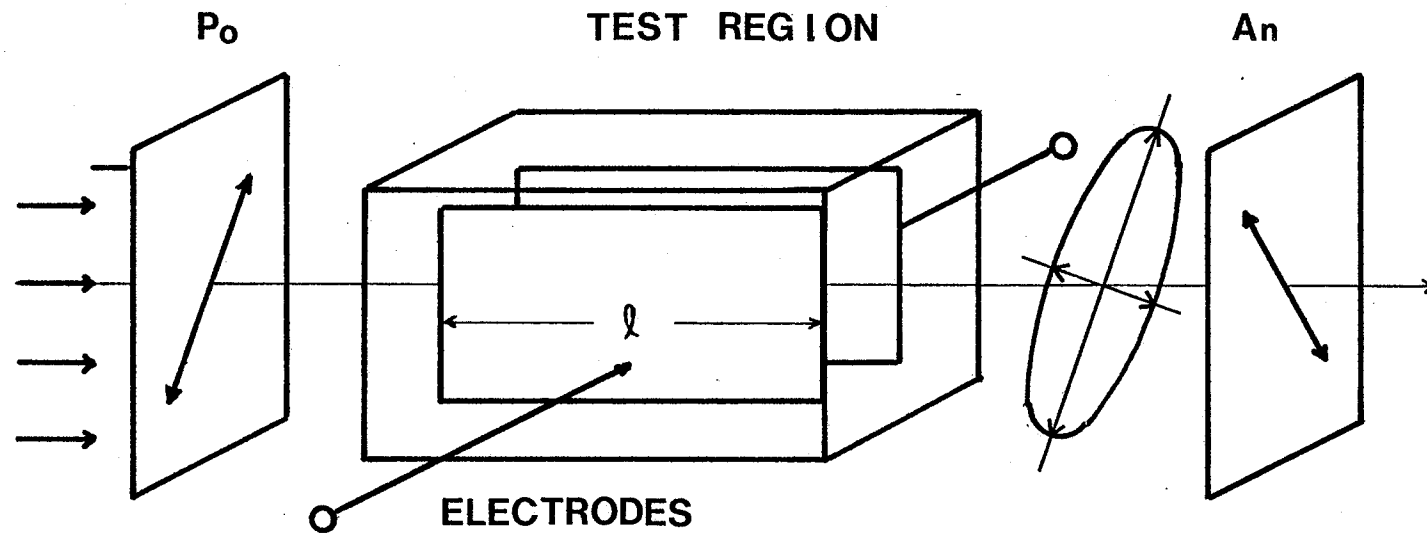
2.1.1 The Kerr-Effect Method

The Kerr-effect method generally used for the measurement of electric field distributions is based on the Kerr-effect. This effect can be observed only in the materials with a field-dependent anisotropy of the refractive index. Although most of dielectric liquids are electrically isotropic, the molecules composing a dielectric liquid are generally anisotropic. Therefore, the molecules under an electric field E can acquire an induced dipole moment P_m , which tends to align with the field. Furthermore, some molecules possess a permanent electric dipole moment P_{m0} which also has the tendency to be orientated by the field E . These orientations, even though opposed by thermal agitation, suffice to render the dielectric optically anisotropic, which would result in a birefringence for the light travelling normal to the direction of the field E . The difference in the principal indices is given by the relation [Denki Gakkai 1974],

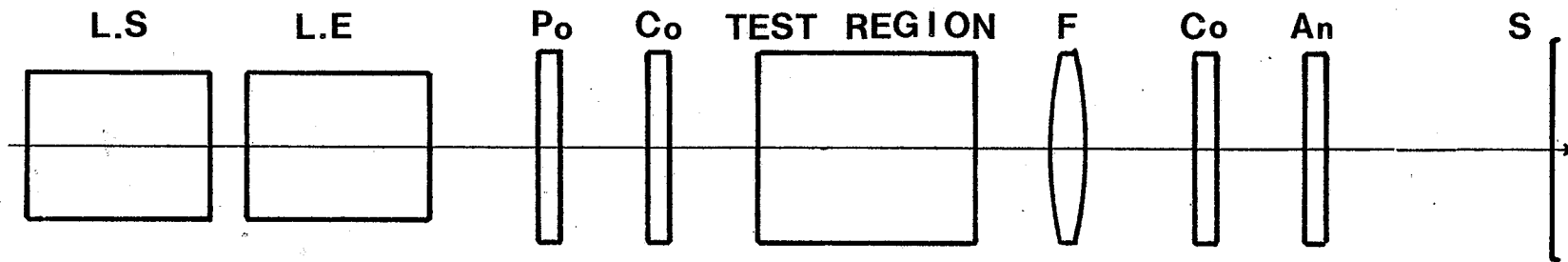
$$n_p - n_n = K_k \lambda E^2 \quad (2.1)$$

where K_k is the Kerr's constant, λ is the wave length, and n_p and n_n are, respectively, the refractive indices corresponding to the directions parallel with and normal to the direction of the electric field. The time constant of the Kerr effect is less than 10^{-9} sec, and therefore it can also be used for a high speed shutter [Denki Gakkai 1978].

The basic optical system based on the Kerr-effect is shown in Fig. 2.1 (A) [Cross and Tobazeon 1973]. The test region (or called the "Kerr cell") is located between a polarizer and an analyzer. The polarizer



(a)



(b)

Fig. 2.1 The basic optical system based on the Kerr-effect. L.S: light source; L.E: light expander; P_0 : Polarizer; C_0 : Compensator; F: Focusing lens; A_n : Analyzer; S: Screen.

gives a coming light beam the polarized angle of 45 degrees against the direction of the electric field in the test region. The components of the polarized light in the directions parallel with and normal to the direction of the electric field travel in the test region with different velocities because the refractive indices n_p and n_n are different. As the result, the initial polarized light changes into an elliptically polarized light, which has a component of the light perpendicular to the initial polarized direction and also a component which increases with increasing electric field. Therefore the electric field can be determined using the analyzer.

If the analyzer is crossed with respect to the polarizer, for example, the intensity I_n of the light transmitted by the analyzer is given by [Cherney and Cross 1973]

$$I_n = I_{no} \sin^2\left(\frac{P_h}{2}\right) \quad (2.2)$$

where I_{no} is the light intensity when the analyzer is parallel with polarizer, P_h is the phase difference introduced by the electric field which is given by

$$P_h = 2\pi K_k L_e E^2 \quad (2.3)$$

in which L_e is the effective length of the optical path in the electric field. In the case of parallel-plane electrode configuration, the effective length L_e can be written as

$$L_e = \ell + \frac{a}{\pi} \left[1 + \frac{a}{\pi} I_n \left(1 + \frac{a}{d} \right) \right] \quad (2.4)$$

where ℓ is the electrode length along the optical pass, d and a are, respectively, the gap length and the thickness of the electrodes. From Equation (2.2), the condition for the transmitted light minima is

$$\frac{P_h}{2} = m\pi \quad (2.5)$$

where m is an integer. Substitution of Equation (2.3) into Equation (2.5) gives the electric field E_k which makes the transmitted light minima, as

$$E_k = \sqrt{\frac{m}{K_k L_e}} \quad (2.6)$$

Thus, the electric field is directly related to the number of m . The electric field E_k corresponding to $m=1$ is denoted by E_{k0} and it is generally called the characteristic electric field of the Kerr-effect in the test cell. The smaller the value of E_{k0} , the higher is the sensitivity of this system.

For the actual system shown in Fig. 2.1(b), an optical compensator is located just after the polarizer and/or also one before the analyzer, and the analyzer is crossed with respect to the polarizer [Cherney and Cross 1973, Cassidy et al. 1974, Durand and Fournie 1970]. The compensator is used to introduce a bias phase P_{ho} for the convenience of the measurement of the electric field or its direction, and the lens system is to project the image in the test region on a screen or a film. A typical fringe pattern is shown in Fig. 2.2. The electric field between the electrodes can be determined by the number of the fringes.

As described before, the sensitivity of this method is mainly

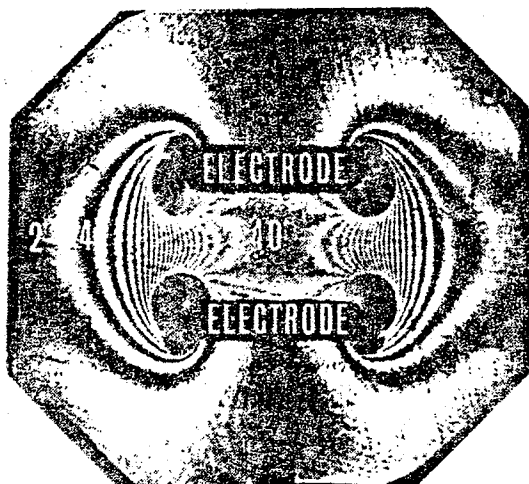


Fig. 2.2 A typical fringe pattern in nitrobenzene photographed (exposure time $0.3\mu\text{s}$) at the peak of a 65.4 kV total-duration $10\mu\text{s}$ pulse. The fact that the field is uniform between the plates is demonstrated by the absence of interelectrode fringe. The side fringes are due to the fringing field along the length of the electrodes.
[after Cassidy, Hebner, Zahn and Sojka 1974].

dependent the Kerr's constant K_k and the effective length L_e . However, for practical measurements, the Kerr's constant K_k is the characteristic of the dielectric liquid under investigation, and the effective length L_e is generally limited to the range from 10 cm to 20 cm for focusing a clear image on the screen. Thus the sensitivity of this method, after all, depends on the Kerr's constant. The Kerr's constant K_k and the characteristic electric field E_{k0} at $L_e = 10$ cm for some dielectric liquids are given in Table 2.1. Only a few dielectric liquids have a Kerr's constant sufficiently large for field measurements. For practical dielectric systems, the Kerr's constant and the effective length L_e are generally not large enough for this method to be used for the detection of any disturbance.

2.1.2 The Doppler Shift Method

The Doppler shift method is generally used for the measurement of flow velocities. The principle of this method is described as follows [Kinbara 1964]; the frequency ν_d of a wave detected by an observer is, in general, different from the frequency ν_s of the source itself, if the observer is not at the same location as the source. For example, if the source is coming up to the observer, ν_d is higher than ν_s , and if the source is going away from the observer, ν_d is lower than ν_s . This phenomenon is called the Doppler shift effect, and in the simplest case as shown in Fig. 2.3, the relation between ν_d and ν_s is given by

$$\nu_d = \nu_s \frac{v_w + v_m - v_d}{v_w + v_m - v_s} \quad (2.7)$$

Table 2.1 The Kerr's constant K_k and the characteristic electric field E_{ko} of some dielectric liquids [after 1978. Rika Nenpyō: *, Denki Gakkai].

Liquid	Symbol	T(°C)	$K_k(\text{cm}^{-1}\text{esE}^{-2})$ [$\lambda = 5461\text{Å}$]	$E_{ko}(\text{kV}\cdot\text{cm}^{-1})$ [$L_e = 10\text{ cm}$]
Carbon disulfide	CS_2	20	3.55×10^{-7}	159
Benzene	C_6H_6	20	0.403 †	473
Toluene	$\text{C}_6\text{H}_5\text{CH}_3$	20	0.714 †	355
Nitrobenzene	$\text{C}_6\text{H}_5\text{NO}_2$	20	396. †	15
Carbon Tetrachloride	CCl_4	20	0.084 †	1035
Hydrogen	H_2	-253	0.0345 †	1615
Oxygen	O_2	-183	0.232 †	622
*Water	H_2O	20	1.32 †	261

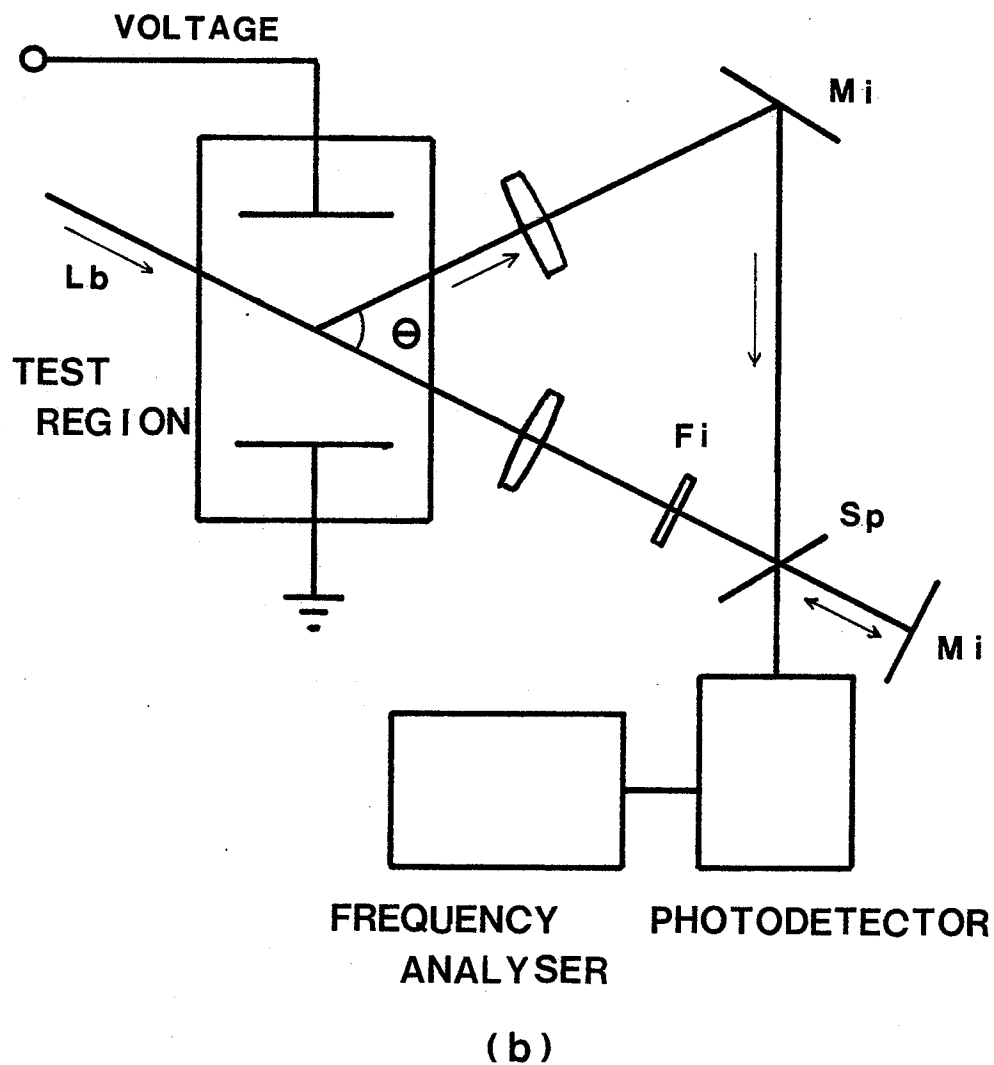
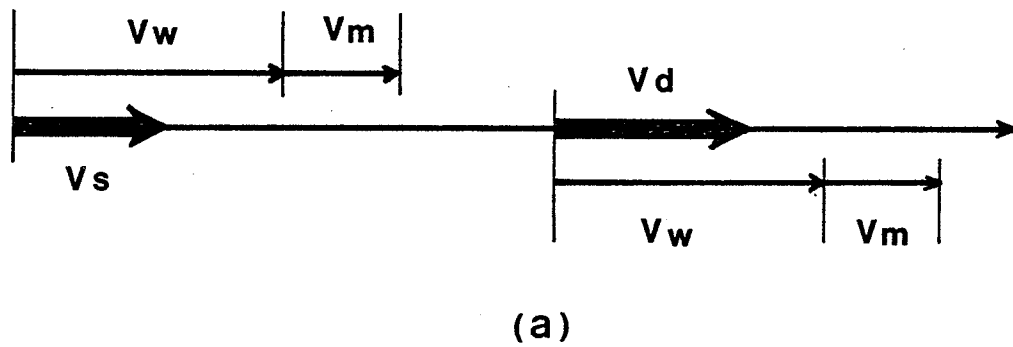


Fig. 2.3 The Doppler shift method. v_w : velocity of a wave in a medium; v_m : velocity of a medium; L_b : laser beam; v_d : velocity of an observer; v_s : velocity of a wave source; mi : mirror; Sp : splitter; Fi : filter.

and the Doppler shift by

$$\Delta\nu \equiv \nu_d - \nu_s = \nu_s \frac{v_s - v_d}{v_m + v_m - v_s} \quad (2.8)$$

where v_w is the velocity of the wave in the medium, v_m is the velocity of the medium, and v_d and v_s are the velocities of the observer and the source, respectively. If the wave is a light beam, Equation (2.8) can be written as

$$\Delta\nu = \nu_s \frac{v_s - v_d}{v_w} \quad (2.9)$$

since v_w in this case is the light velocity which is much larger than v_s . Usually, the frequency ν_s , and the velocities of the light and light source are known, thus the relative velocity between the observer and the light source can be determined.

The actual optical system for the Doppler shift method is shown in Fig. 2.3(b). The light source is a laser which can produce a high coherent light beam for the accurate measurement of the Doppler shift, and hence it is sometimes called the laser Doppler shift method. The light beam is scattered mainly due to the particles in the fluid under investigation. This scattered light having the velocity information is mixed with the initial light beam on a splitter to extract the Doppler shift from the frequency of intensity modulation. In this system, the Doppler shift is given by,

$$\Delta\nu = \frac{v_s}{v_w} \nu_d \{(1 - \cos 2\theta) \cos\theta + \sin 2\theta \sin\theta\} \quad (2.10)$$

and therefore the velocity is

$$v_d = \frac{v_w}{v_s} \times \frac{\Delta v}{(1 - \cos 2\theta) \cos \theta + \sin 2\theta \sin \theta} \quad (2.11)$$

where θ is the angle between the direction of laser beam and that of the scattering light as shown in Fig. 2.3(b).

Generally, for the laser Doppler shift method, the particles are necessary in order to obtain the full intensity of scattering light, since the scattering cross-section of molecules are some twenty orders of magnitude less than that normally required for the system [Poulter and Snaddon 1978]. Therefore, sometimes a small amount of particles is added into the flow to improve the sensitivity [Usuda and Sakamoto 1977, Poulter and Snaddon 1978].

Using the laser Doppler shift method, the particle velocity in the fluid can be measured rapidly, objectively and non-invasively. These advantages make it an ideal method for investigating the transport process of fluids in non-electrical living system, since the particles in such a system can be expected to follow the flow of the host fluid easily. In dielectric liquids, however the particles can also move with the influence of an applied electric field. If dielectric particles are added in dielectric liquids to improve the sensitivity, they would experience the electrostatic and electromechanical forces under electric fields. In this case the net force F on a spherical dielectric particle of radius r in a dielectric liquid is given by

$$\begin{aligned} F &= \text{electrostatic force} + \text{electromechanical force} \\ &= Eq_p + \frac{\pi}{32} r^3 \epsilon_0 \epsilon_p \left(\frac{\epsilon_p - \epsilon}{\epsilon_p + 2\epsilon} \right) \text{grad } E^2 \end{aligned} \quad (2.12)$$

where ϵ_0 , ϵ_p and ϵ are, respectively the dielectric constants of vacuum, the particle and the fluid; and q_p is the charge of the particle .

These forces cause the error for the measurement of the velocities of such a flow created by hydrodynamic motion. In order to reduce these forces, it is necessary to use particles having a dielectric constant same as that of the dielectric liquid and having a size as small as possible provided that they can give a large enough scattering cross-section.

2.2 Electric Field Distributions in Dielectric Systems

For linear, homogeneous and isotropic media, the electric field distributions can be determined by means of electrolytic tanks or impedance meshes by analogy, or calculated by means of numerical computations. However, such ideal dielectrics do not exist in practice. For practical materials, the field distribution is not only dependent on their physical parameters (such as dielectric constants and conductivities, etc.) and the geometric arrangement of electrodes; but also on the field dependence of these physical parameters and, the worst of all, on the space charge and the liquid motion effects [Filippini et al. 1970, Denki Gakkai 1974]. All of these factors make the determination of the field distribution by means of computation alone or other analogy methods for practical cases almost impossible. However, the field distributions in practical dielectric systems have been measured using a movable metallic probe, the Kerr-effect and other methods. In the following, the field distributions for two cases in steady states (i) the field distributions between parallel-plane electrodes; and (ii) the field distributions along a dielectric solid are discussed.

2.2.1 The Electric Field Distributions Between Parallel-Plane Electrodes

For practical dielectric liquids, the electric field distributions between parallel-plane electrodes are, in general, nonuniform due to the presence of space charge. In other words, the distribution profiles are controlled by the factors which control the space charge distributions. For example, based on the measurements by using the Kerr-effect method, Cassidy et al. [1974] has demonstrated that the electric field distributions in nitrobenzene are dependent on the magnitude and the frequency of the applied voltage, the electrode material and their surface conditions, and the immediate previous history of the system.

Impurities in dielectrics, in general, act as one of the source of the charge carriers, and hence the cause of the space charge. Cherney and Cross [1973] have reported the dependence of the static electric field distribution on dissolved water and air for two different chlorobiphenyls (Aroclor 1242 and 1016). The results obtained using the Kerr-effect method show that the dissociation of the water molecules results in an exponential distribution of positive space charge giving rise to an enhanced cathode field, and that the presence of air tends to decrease the cathode field. These results fully indicate the effect of impurities on the field distributions. In practical dielectric systems without using special purification techniques, water and gases (air) are always involved as impurities, and therefore they cause unreproducible results not only for the determinations of electric field distributions but also for the measurements of conduction currents [Prabhakara 1970].

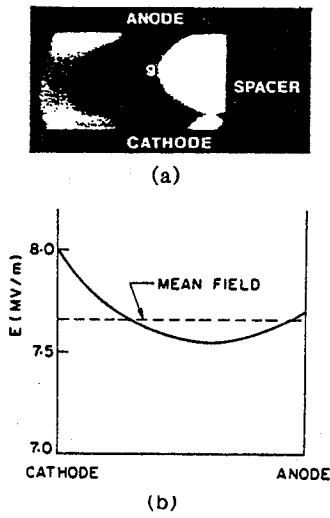
The electric field itself also changes its distribution profiles. In the steady-state, this effect is mainly due to the charge generation in the bulk and charge injection from electrodes. The first cause involves the aforementioned dissociations of impurities and " α -process" similar to the Townsend model for increasing the conduction current in gases. For the charge injection from electrodes, this effects partly depends on the electrode material itself or depends on the electrode surface conditions. Eldine et al. [1964] have studied the influence of electrodes coated with a pore-free film on the steady-state potential distributions in transformer oil, and shown that the coated electrodes enhance the electric field near the electrodes. And Cassidy et al. [1974] have also measured the electric field distributions in nitrobenzene both for the glass-blasted nickel electrodes and for the electro-polished stainless steel electrodes under dc and ac (40 ~ 200 Hz) electric fields. Although these experimental results show the dependence of the field distribution on the electrode materials or their surface conditions, the relation between the field distribution and the conditions of electrode is still not fully understood.

The electric field distributions not only change with aforementioned factors but also change with the sort of dielectric liquids. According to Forster [1964]; for saturated hydrocarbons such as n-hexane, n-heptance, etc., the electric field distributions at the average fields between 50 and 1 kv/cm are approximately symmetrical with respect to the electrodes; but for unsaturated hydrocarbons the distributions are rather asymmetric, although the field became higher near electrodes, and they change gradually with time in the order of hours. From the measurements of conductivities

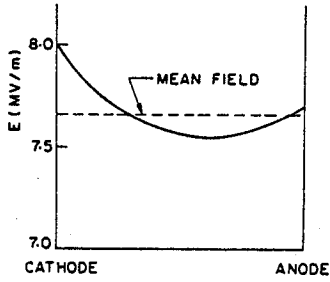
he attributed the difference to their conduction processes, because unsaturated hydrocarbon molecules can easily form positive ions by losing their π electrons.

2.2.2 The Electric Field Distributions Along a Dielectric Solid

In general, the electric field distributions along a dielectric solid are different from that in the dielectric liquid itself. Cross and Tobazeon [1973] have reported such electric field distortions introduced in a uniform field gap in nitrobenzene by various dielectric spacers bridging the gap. Their typical results are shown in Fig. 2.4. Obviously, it can be seen that the electric field distribution profiles along the spacers are different from the other areas, and also depend on the material. Cross and Tobazeon [1973] have attributed these distortions to the space charges in the solid or to an uneven distribution of the charges on the solid surface because of the slow response for the establishment of a steady-state distortion and its dependence on the natures of the solid. On the other hand, Cherney and Cross [1974] have shown that, using the same experimental techniques but for chlorobiphenyl of commercial purity, the field distortions are independent of the electrical properties of the dielectric solids and applied voltage. They have suggested from their measurements of the surface current density that the distortions are created by the electrohydrodynamic motion of the liquid near the interface. Although, there is a discrepancy between their explanations for the field distortions, both of them have reported that the enhancement of the electric fields are too small to account for the weaker dielectric strength along the interface.

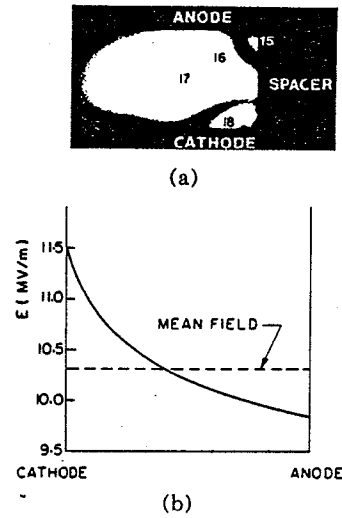


(a)

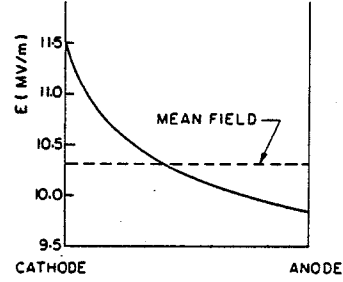


(b)

a; (a) Kerr fringes for a polyethylene spacer separating electrodes in nitrobenzene. (b) Field distribution at the spacer surface shown.

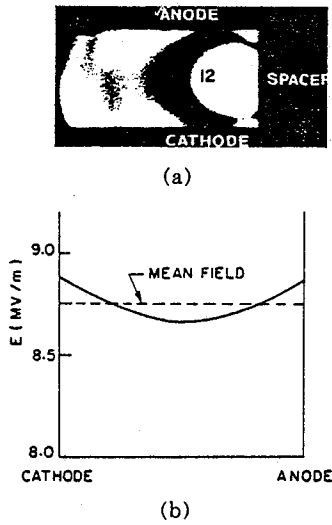


(a)

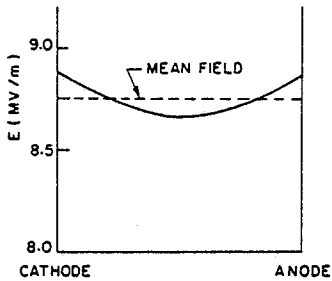


(b)

c; (a) Kerr fringes for a nylon spacer separating electrodes in nitrobenzene. (b) Field distribution at the spacer surface shown.

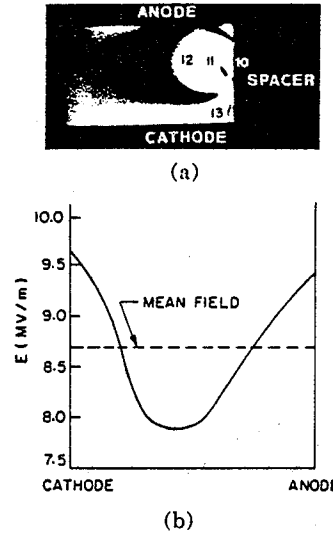


(a)

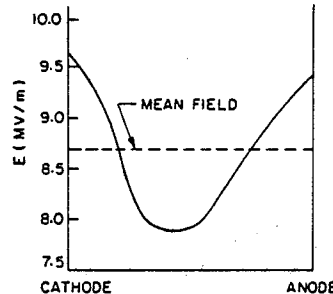


(b)

b; (a) Kerr fringes for a Teflon spacer separating electrodes in nitrobenzene. (b) Field distribution at the spacer surface shown.



(a)



(b)

d; (a) Kerr fringes for a barium titanate spacer separating electrodes in nitrobenzene. (b) Field distribution at the spacer surface shown.

Fig. 2.4 Electric field distortions introduced in a uniform field gap in nitrobenzene by various dielectric spacers bridging the gap [after Cross and Tobazeon 1973].

2.3 Disturbances in Electrically Stressed Dielectric Liquids

The major disturbances in electrically stressed dielectric liquids are electrohydrodynamic motion, electrostriction, space charge distribution, prebreakdown and breakdown phenomena. Previous work in this area has made considerable progress toward the understanding of these dielectric phenomena, especially, those relevant to breakdown. In the following we shall confine ourselves to the subjects of electrohydrodynamic motion, prebreakdown and breakdown phenomena.

2.3.1 Electrohydrodynamic Motion

It is well known that fluid dielectrics, in general, move under the influence of an electric field. This phenomenon called the electrohydrodynamic (EHD) motion has been attributed to two mechanisms; (i) the momentum transfer from the charge carriers which move in the electric field to the neutral molecules; and (ii) the electromechanical force created by the field resulting from the spatial variation of the dielectric constant. For mechanism (i), the charge carriers are mainly due to ions or ion complexes, and for mechanism; (ii) the spatial variation of the dielectric constant can arise by the spatial variation of temperature or contamination. Thus the resultant force F can be written as [Cherney and Cross 1974]

$$F = \nabla q_d \times E - \nabla(E^2/2) \times \nabla \epsilon \quad (2.13)$$

where ∇ is the gradient operator, and q_d is space charge density.

In fact, Faraday was the first to notice this phenomenon, and he found that the speed of motion increased with increasing current. However,

this phenomenon did not receive much attention as a significant conduction process in dielectric liquids until about 1956. In 1956, Ostromov observed the liquid motion in benzene and transformer oil between parallel plane-plane electrodes using a Schlieren optical technique, and that the current increased when the motion changed from a laminar flow to a turbulent flow. Since then, a great deal of experimental and theoretical work has been done in order to clarify the characteristics of the electrohydrodynamic motion and to study the mechanisms of charge carrier production at electrode surfaces as well as in the bulk by means of this liquid motion phenomenon.

The general features of the electrohydrodynamic motion are: (i) the speed increases with increasing input power [Essex and Secker 1969]; (ii) the speed is proportional to E for single injection and E^2 for double injection; (iii) the speed is largely dependent on the electrode configuration and the shape of the test cell [Gray and Lewis 1969]; (iv) the direction of the motion is from one electrode (carrier source) to the other (carrier collector) [Gray and Lewis 1965]; (v) the absorbed gas tends to increase the speed [Dey and Lewis 1968, Nelson and McGrath 1972]. The more details about the liquid motion have been reported by Filippini et al. [1970]. They have studied the development of flow streamer between electrodes in deionized nitrobenzen and chlorobiphenyls by using the high speed Schlieren technique and the Kerr-effect. The interesting feature, according to their results, is that the development of flow has the shape similar to a filamentary conduction channel as mentioned by Kao [1975, 1976] in his filamentary single injection theory for high field electric conduction

and breakdown in dielectric liquids. Recently, several investigators have obtained some basic data on the onset of fluid instability and the development of the flow streamer between electrodes [Felici 1969, Hakim and Higham 1962].

One of the important effects of the liquid motion is to modify the effective mobility of charge carriers. Gray and Lewis [1965] and Secker and Lewis [1965] have shown this effect experimentally, and suggested that this motion must be considered as a source of errors for the measurements of true carrier mobilities. By taking into account the effect of the liquid motion, Gray and Lewis [1969] have deduced from their measurement of ionic mobilities a true ion mobility in n-hexane, which is $1.8 \times 10^{-4} \text{ cm}^2 \text{V}^{-1} \text{S}^{-1}$ at 20°C. However, this value is about five times smaller as compared with the normally accepted value of $10^{-3} \text{ cm}^2 \text{V}^{-1} \text{S}^{-1}$ [Terlecki 1962]. Nowadays, many investigators [Filippini et al. 1970, Nelson and McGrath 1972, Cherney and Cross 1974, 1977, Kao 1976, Forster and Wong 1977] believe that the electrohydrodynamic motion would modify the apparent carrier mobility and indirectly affect the conditions for electric conduction and breakdown in dielectric liquids.

Regarding the motion caused by the spatial variation of the dielectric constant, the literature is comparably scarce. Watson [1961] has reported that an applied electric field enhances the apparent heat conductivity from a heated electrode to a dielectric liquid. Nelson et al. [1972] have used this effect to study the polarity effect for the motion induced by charge carriers, and Savkar [1972] has studied this effect by using alternating electric fields. Although the electro-

mechanical force created by the field resulting from the spatial variation of the dielectric constant is well known, the liquid motion due to this force is still not fully understood.

2.3.2 Prebreakdown Phenomena

Since Hakim and Higham [1961] and Farazmand [1961] have reported that the breakdown in n-hexane under highly divergent electric fields was preceded by the growth of a region having a different refractive index, a number of investigators have studied such a disturbance for various dielectric liquids under various experimental conditions in order to study the prebreakdown and breakdown processes in dielectric liquids. Some typical results for the growth of such disturbance regions in transformer oil [Morikawa 1972] and in liquid nitrogen [Murooka and Sueda 1976] are shown in Fig. 2.5. From these high speed Schlieren (or shadowgraphic) photographs, we can observe the transient behavior of the prebreakdown disturbance in a short period from the application of the voltage to the final breakdown.

The general characteristics of the disturbance may be summarized as follows: (i) it requires a formation time which is of the order of μ seconds [Yamashita et al. 1977, Morikawa 1972, Forster and Wong 1977]; (ii) the disturbance has a shape like a bush for the disturbances started either from a positive or from a negative point electrode, the individual branches are much more sharply defined for the positive one [Morikawa 1972, Heiman et al. 1976, Yamashita et al. 1977]; (iii) the propagation velocity is much faster for the disturbance originated at the positive point than that at the negative one [Morikawa 1972, Yamashita et al.].

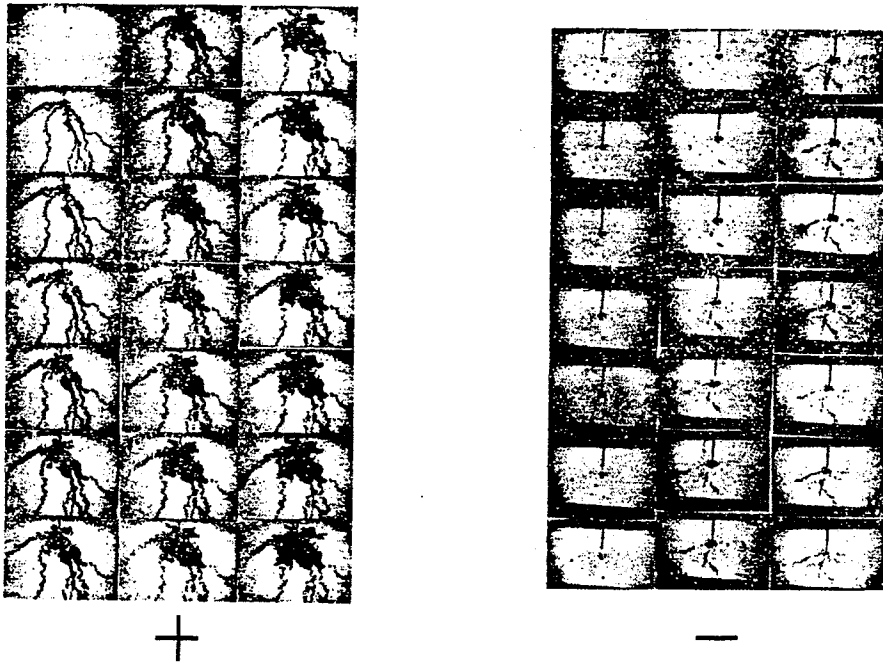


Fig. 2.5(a) The photographs of propagation of prebreakdown disturbances, produced by the impulse breakdown between point-plane electrodes in dielectric oil. These pictures were taken by Schlieren method, using a xenon flash lamp and a Beckman camera. Applied voltage: 36 kV, $1 \times 140\mu\text{s}$, frame separation: $66.5\mu\text{s}$, exposure time: $3.6\mu\text{s}$, pressure: 0.5 mm Hg, gap length: 25.4 mm [after Morikawa 1972].

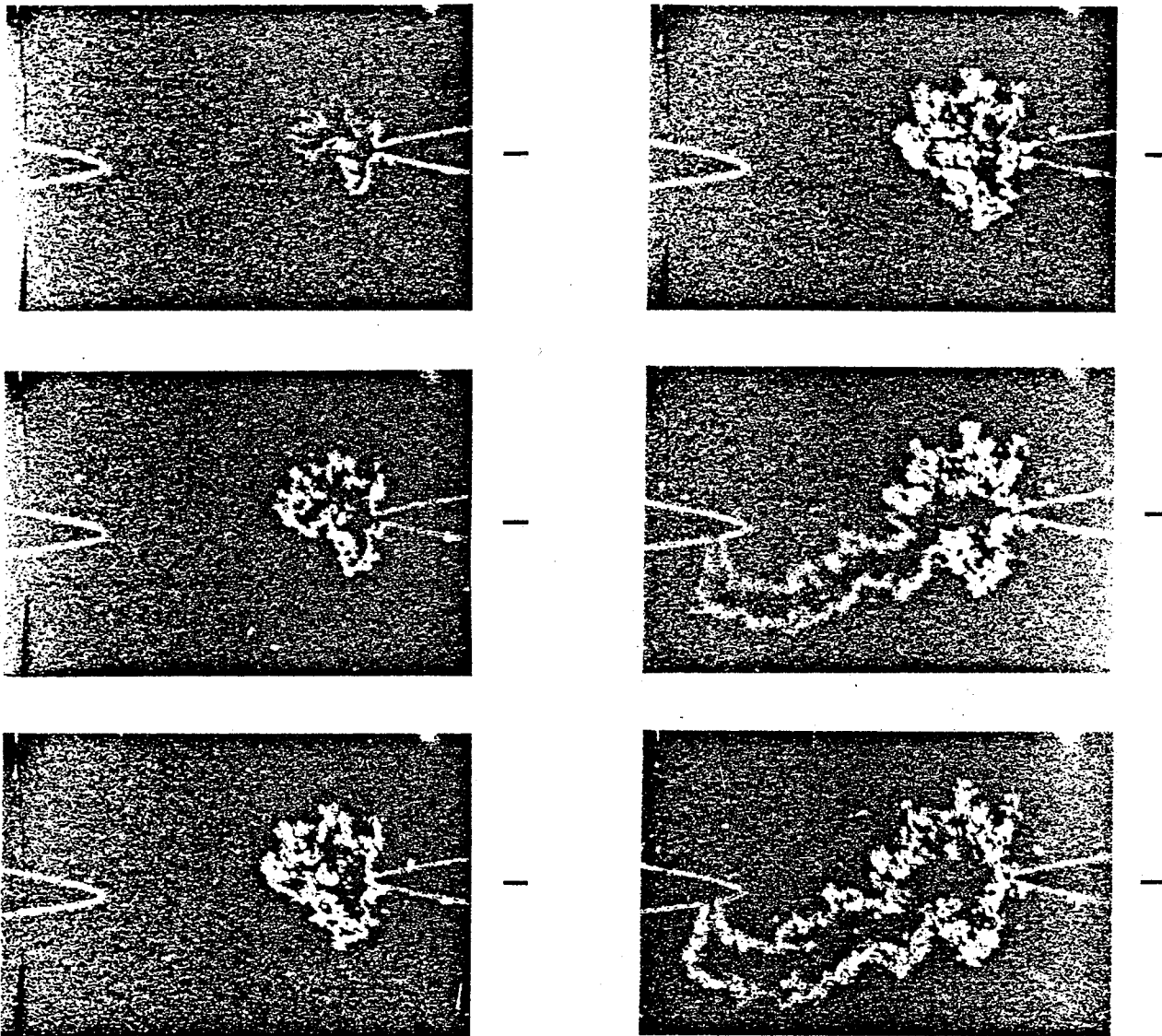


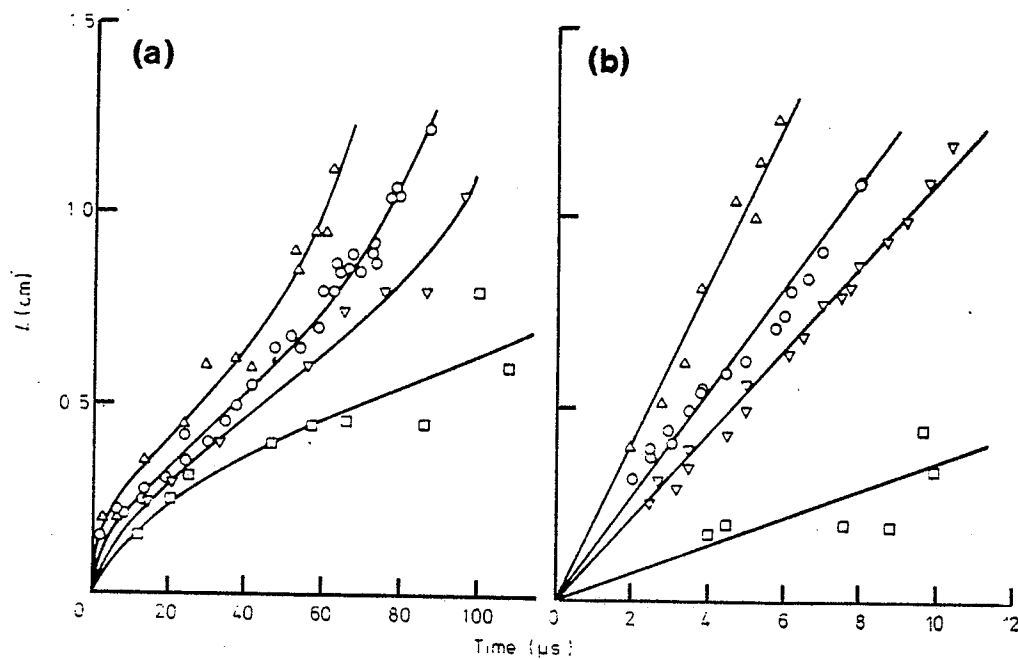
Fig. 2.5(b) The photographs of propagation of prebreakdown disturbances produced by the impulse breakdown between point-point electrodes in liquid nitrogen. These pictures were taken by Schlieren method using a ring edge. Temperature -196°C , pressure 1 atm, gap length 6 mm, applied impulse voltage 58kV, [after Murooka and Sueda 1976].

Fig. 2.6 shows the length of the disturbance in white oil as a function of time [Devins et al. 1976]; (iv) the disturbance scatters the incident light [Singh et al. 1972, Nelson and Hashad 1976]; (v) the disturbance is accompanied with shock waves, current pulses and light emission [Yamashita et al. 1977, Murooka and Sueda 1976, Chiu 1976, Morikawa 1972, Heiman et al. 1976, Forster and Wong 1977].

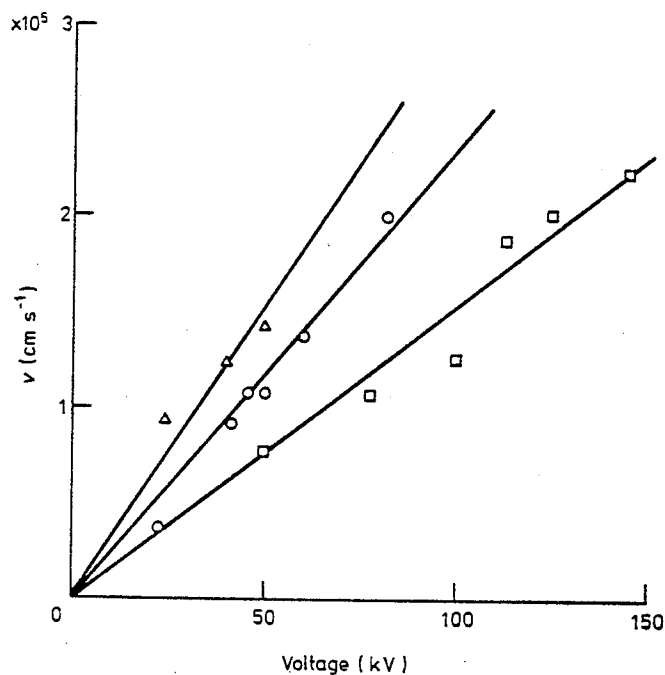
(A) The nature of the disturbance.

Several models have been put forward about the nature of the disturbance, and they are: (i) it is due to the plasma which produces a high temperature region in the liquid [Chadband and Calderwood 1972, Allan and Hizal 1974, Heiman et al. 1976]; (ii) it is a gas phase composed of micro-bubbles in the liquid [Morikawa 1972, Thomas and Forster 1975, Nelson and Hashad 1976, Forster and Wong 1977].

For the negative disturbance, Yamashita et al. [1977] have proposed that electrons are emitted from the point cathode and possess energies sufficiently large to collide with liquid molecules, and to produce molecules of lower molecular weight by electrochemical dissociation in the high field region. These molecules could be CH, H₂, C₂ and CH⁺. It seems likely that these molecules are locally concentrated and change into a gaseous phase when the saturation point in the liquid is exceeded, and at that instant, shock waves also ensue. The gaseous phase forms a conductive channel of plasma state and results in a change in density observed. For the positive disturbance, liquid molecules in the highest field region near the point can lose electrons which are rapidly accelerated into the needle point. This action may induce the dissociation of the liquid



A ; Length of streamer as a function of time. Gap=1.27 cm. (a) negative point: Δ 185 kV; \circ 155 kV; ∇ 125 kV; \square 100 kV. (b) positive point: Δ 82 kV; \circ 60 kV; ∇ 46 kV; \square 23 kV.



B ; Positive streamer velocities as a function of voltage for three different gaps. Δ 0.64 cm; \circ 1.27 cm; \square 2.54 cm.

Fig. 2.6 Velocities of prebreakdown disturbances in white oil [after Devins, Rząd and Schwabe 1976].

molecules and a change in density in the same manner as for the negative disturbance. Yamashita et al. [1977] have attributed the initiation to the gaseous phase caused by electrochemical dissociation. This hypothesis fits well to the spectral analysis for the prebreakdown phenomena in transformer oil reported by Morikawa [1972] and Murphy [1970]. A similar model has also been suggested by Morikawa [1972] and Toriyama [Denki Gakkai 1974]. However, in the case of the dielectric liquids composed of mono atomic molecules such as liquid nitrogen, oxygen and helium; the molecules will not be dissociated to gaseous phase by the emitted electrons although they are heated up and evaporated. Thomas and Forster [1975] and Forster and Wong [1977] have attributed the initiation to the heat energy associated with the conduction current injected from local asperities on the cathode surface.

It is interesting to note that the final breakdown does not always occur even though both the electrodes have been bridged by the disturbance. This suggests that the disturbance is not necessary to be a conductive channel or plasma. In fact, the disturbance shown in Fig. 2.5(a) looks like a region composed of cold microbubbles or the charge carrier traces which could be observed in a bubble chamber [Murooka and Toriyama 1974]. Nelson and Hashad [1976], Singh et al. [1972], and Krasucki [1966] have treated the disturbance simply as a region composed of microbubbles of sizes of the order of microns in diameter. Their models can explain some prebreakdown and breakdown phenomena.

(B) Dependence of hydrostatic pressure.

Morikawa [1972] has reported the dependence of the prebreakdown

disturbances in filtered and degassed transformer oil on hydrostatic pressure. The effects of pressure on the propagation velocity of the disturbance and on the corona inception voltage are, respectively, shown in Fig. 2.7 and Table 2.2. It can be seen that the propagation velocity decreases slightly when the pressure is increased, and on the other hand, the corona inception voltage increases with increasing pressure. The Schlieren images can be observed only when the corona is observed [Morikawa 1972], implying that the disturbance occurs and propagates more easily at low hydrostatic pressures. This also indicates that the disturbance is in a gas phase.

(C) Dependence of additives.

Devins et al. [1976] have reported that the additives such as various polyaromatic compound in white oil affects the propagation characteristics for the positive and negative disturbances as shown in Fig. 2.8. Both the velocities of the positive and negative disturbances increase with increasing concentration of the additives. Polyaromatic compounds have two physical properties; low ionization potentials and large electron trapping cross-sections. In order to distinguish the effects between the low ionization potentials and large electron trapping cross-sections, Devins et al. [1976] have also studied these effects for N, N-dimethylaniline which does not trap electrons but has an even lower ionization potential than 2-methyl naphthalene, and for sulphur hexafluoride which has a high ionization potential and large trapping cross-section. Their results are shown in Fig. 2.8(b). It is clear that the increase in the velocity of negative disturbance is due to electron trapping. This means that, for

Table 2.2 Pressure dependence of corona inception voltage in the dielectric oil [after Morikawa 1972].

Exp. condition		Pressure		
		0.05mmHg	1.0mmHg	760mmHg
Intense corona inception volt.* (kV)	Needle: pos.	17.2	17.9	19.0
	Needle: neg.	23.7	24.1	29.4
Corona inception voltage* (kV)	Needle: pos.	15.5	16.0	18.2
	Needle: neg.	22.6	23.1	29.2
50% corona voltage** (kV)	Needle: pos.	15.7	15.6	17.6
	Needle: neg.	22.0	22.5	28.1

*Minimum value

**Corona appears more than 5 out of 10 discharges

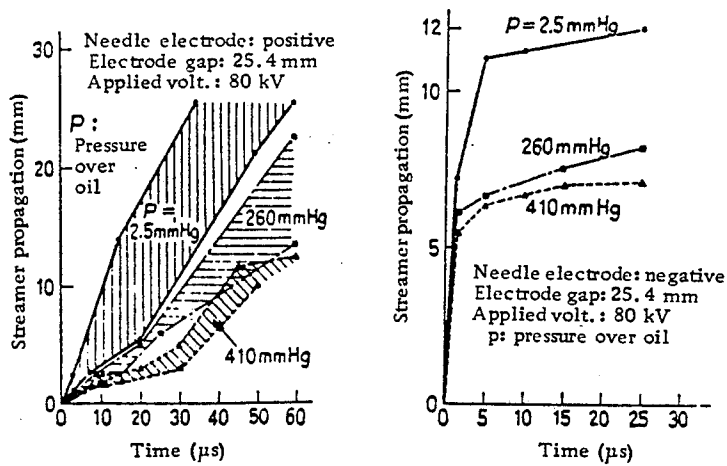
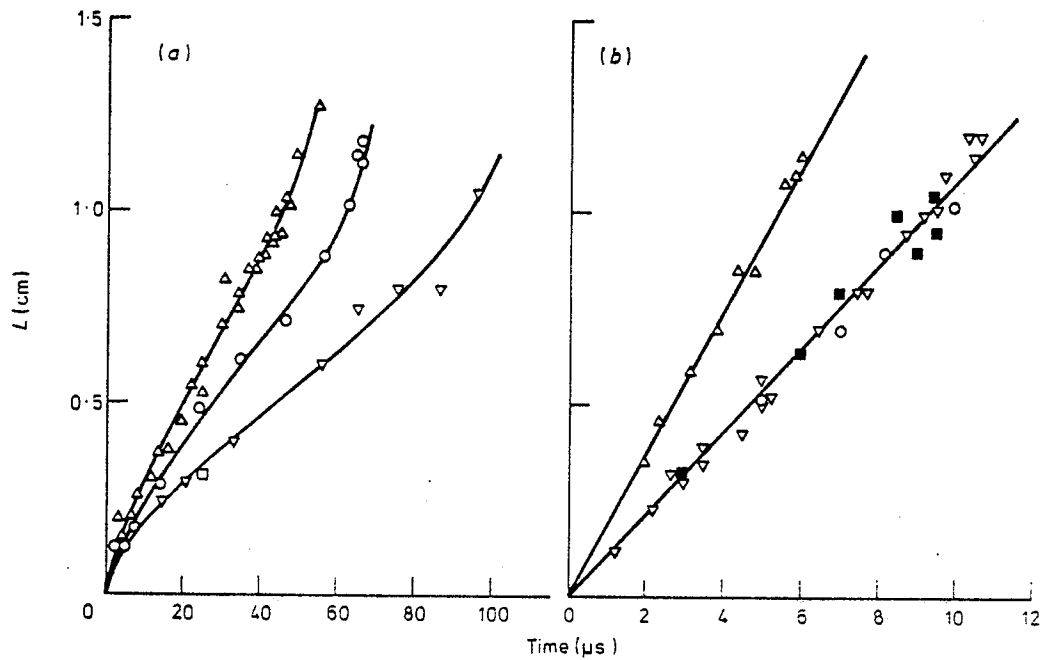
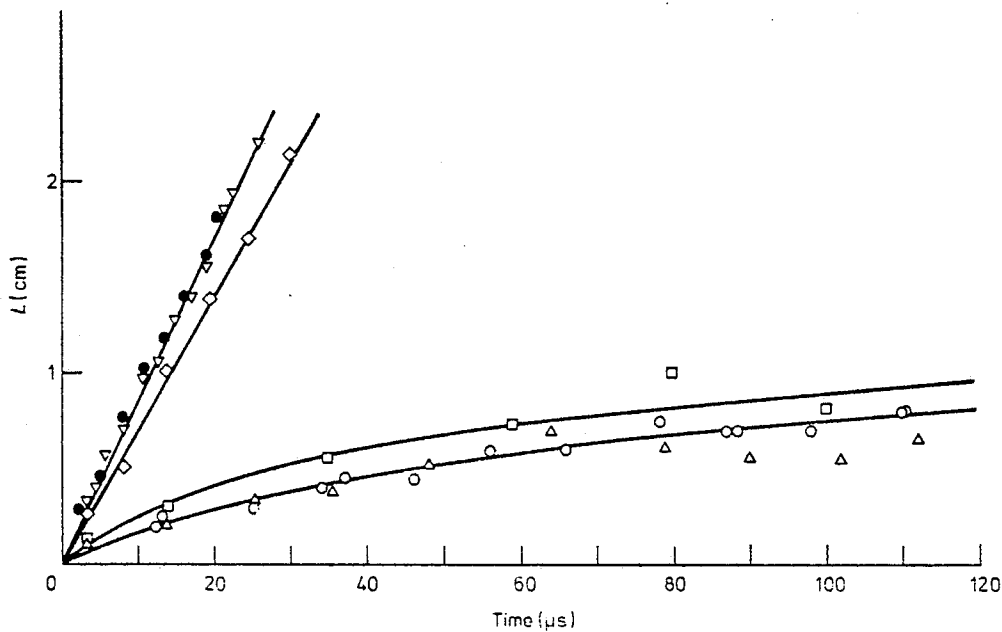


Fig. 2.7 The effects of pressure on the streamer propagation [after Morikawa 1972].



The effect of 2-methyl naphthalene on the streamer propagation rates. Gap=1.27 cm. (a) negative point, 125 kV: ∇ pure Marcol 70; \circ 7.3×10^{-3} M and \triangle 7.3×10^{-2} M 2-methyl naphthalene. (b) positive point, 46 kV: ∇ Pure Marcol 70; \circ 7.3×10^{-3} M and \triangle 7.3×10^{-2} M 2-methyl naphthalene. The solid squares \blacksquare refer to a nitrogen-saturated solution.



The effect of several additives on the negative streamer propagation rates. Gap=2.54 cm, voltage=150 kV. \circ pure Marcol 70; \square 0.158 M N,N' -dimethylaniline; \triangle 2×10^{-3} M ethyl chloride; \diamond 6×10^{-3} M ethyl chloride; \bullet 2.4×10^{-2} M ethyl chloride; ∇ 2.1×10^{-2} M sulphur hexafluoride.

Fig. 2.8 The effects of additives on the propagation rates.

the negative disturbance, the ionization process is less important than the trapping process. Their results are indirectly in support of the formation of microbubbles due to the electrostatic forces created by the high concentration of negative charge. For the positive disturbance, the electron scavengers have negligible effect on the velocity but the dimethylaniline which has a lower ionization potential enhances the velocity to the same extent as does the 2-methyl naphthalene. This indicates that the ionization process is important for the positive disturbance.

(D) Dependence of viscosity.

Krasucki [1966] has studied the prebreakdown phenomena in hexachlorodiphenyl. The viscosity of this liquid is 6×10^6 P at 17.5°C and it decreases rapidly with increasing temperature and becomes 2P at 75°C . He has directly observed the prebreakdown disturbance by using a microscope, and reported that, even in a parallel-plane electrode configuration of 0.1 mm in gap length, the propagation or growing velocity was so slow that it can be recorded by using an ordinary movie camera of 16 frames per second. He has regarded this disturbance as a vapour bubble, and suggested that vaporization is initiated by the development of points of zero pressure resulted from the presence of submicroscopic particle impurities in the liquid. According to his hypothesis, if the breakdown in a liquid results from the formation and growth of the vapour bubbles, the time to breakdown should highly depend on the viscosity of the liquid. In fact, according to his experimental results [Krasucki 1966], it has been shown that the time to breakdown for hexachlorodiphenyl is almost directly proportional to the viscosity over the six order.

However, Krasucki has not fully discussed the energy for producing such a vapour bubble.

2.4 Breakdown Processes

Many theories have been put forward for the breakdown processes in dielectric liquids, but still there is no one theory which satisfies all the experimental results. Broadly speaking, these theories can be grouped into three categories; (i) based on the electron multiplication process; (ii) based on the bubble formation; and (iii) based on suspended particles in a dielectric liquid. Electron multiplication process is that an electron, on the average, makes ionizing collisions and builds up an electron avalanche in the liquid. Thus this theory is based on the hypothesis that an electron can obtain enough kinetic energy for ionized collisions in the breakdown field than the energy would lose to many types of non-ionized collisions [Sharbaugh et al. 1978]. Lewis [1956] and Adamezewski [1969] have modified the breakdown criterion proposed originally by von Hippel [1937] for ionic crystals, and succeeded to explain the dependence of breakdown strength of hydrocarbon liquids on their molecular structures. However, their theory has the difficulty to explain the dependence of the breakdown strength on hydrostatic pressure. In fact, the possibility of the electron multiplication process in high-density media such as liquids is doubtful. As has been pointed out by Kao and Rashwan [1974], the mean free path of an electron in dielectric liquids is of the order of 10^{-7} cm. It is hard to believe that an electron can gain a kinetic energy of the order of 1 - 7 eV to excite an atom or a

molecule, and of the order of 10 - 20 V to ionize an atom or a molecule even at a field of 10^6 V/cm.

On the other hand, the breakdown theories based on the bubble formation have been developed to overcome the difficulties of aforementioned process by Kao [1975, 1976] and Sharbough and Watson [1962]. This process obviously fit well for the prebreakdown phenomena in high viscosity materials as shown by Krasucki [1966]. This process will be described later. The breakdown process based on the suspended particles is important for the breakdown in commercial liquids such as transformer oil which usually contains a high concentration of impurity particles. Kok [1961] has proposed a breakdown theory based solely on particle effects. According to their theory the breakdown is due to the formation of a string of particles which are accumulated in the electrode gap due to electromechanical force. This introduces a dependence of breakdown strength on time, concentration and size of particles, and the liquid viscosity.

It is most likely that the so-called intrinsic breakdown does not exist in liquids. Breakdown in liquids is extrinsic via some secondary mechanisms. The most important mechanism may be the bubble formation process.

Kao and Higham [1961] have investigated the effect of hydrostatic pressure on the breakdown strength of various organic liquids, under well controlled conditions. Their results are shown in Fig. 2.9. Obviously, it can be seen that the breakdown strengths increase with increasing hydrostatic pressure. Since the electron multiplication process is directly governed by the mean free path of an electron, it is hard to reconcile this process with the pressure dependence on nearly incompressible liquids. Such a pressure dependence does, however, suggest strongly that there is a change

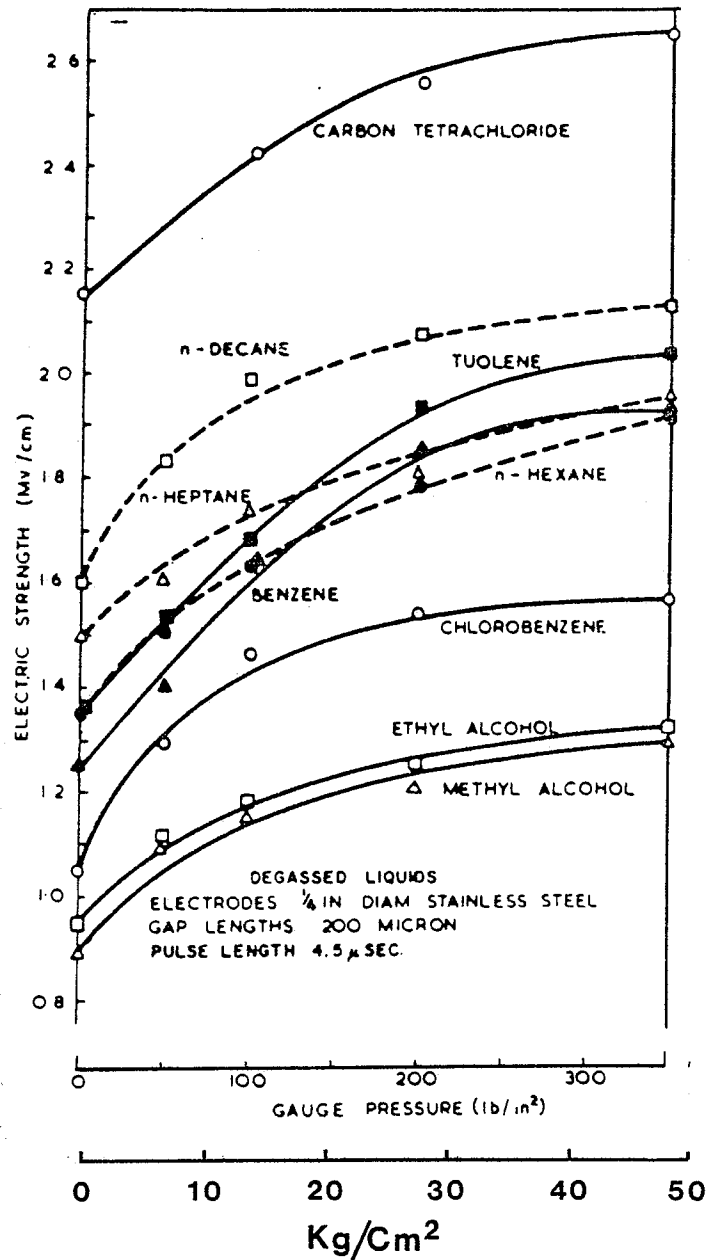


Fig. 2.9 The dependence of breakdown strength of some organic liquids on applied hydrostatic pressure [after Kao and Higham 1961].

of phase (or formation of a bubble) during some step in the breakdown process.

Kao has proposed in 1965 that bubbles may be formed in the liquid by the following processes, (i) from the gas which accumulates in microscopic activities on the electrode surface; (ii) from the liquid itself by local evaporation on the surface of the electrodes; (iii) due to electrostatic forces overcoming the surface tension. Also, the electric dissociation proposed by Yamashita et al. [1977] may be considered as one of the processes. Once these bubbles or low density regions have formed, the mean free path of an electron will be effectively increased. As the result, breakdown would be expected to follow rapidly in these low density regions.

Sharbaugh and Watson [1962] have proposed a thermal mechanism in order to explain the pressure dependence observed by Kao and Higham [1961]. By assuming that a bubble of liquid vapour is formed by injection of large-power electron densities from asperities on the cathode, they have derived the breakdown criterion based on the balance condition between the heat needed for vaporization and the input energy as

$$CE_b^n t = C_p(T_b - T_0) + L_v \quad (2.14)$$

where n is a factor in the range 1.5 to 2, t is the duration of the application of voltage, C_p is the specific heat at constant pressure, T_b and T_0 are, respectively, the boiling point and the initial temperature of the liquid, and L_v is the latent heat for vaporization. Since the boiling point of the liquid increases with increasing applied pressure, Equation (2.14) shows clearly the pressure dependence of breakdown voltage.

Their computed results based on this equation for breakdown strength as a function of pressure are in good agreement with the experimental results of Kao and Higham [1961].

Kao [1975, 1976] has recently put forth a new theoretical model (called a filamentary single injection model) for breakdown in dielectric liquids. This model is based on the postulates that near breakdown there is only one filament in which the current density is large enough to cause vaporization of the liquid. Thus the criterion for breakdown is expressed in the form of a current-temperature balance equation in a filament. He has obtained the expression for the breakdown strength under pulse conditions as

$$E_b = \left[\frac{8}{9} \frac{C_p \rho k d}{W \epsilon v_0 M_\tau} \cdot \left\{ T_0^2 \exp\left(\frac{W}{K T_0}\right) - T_b^2 \exp\left(\frac{W}{K T_b}\right) \right\} \right]^{\frac{1}{3}} \quad (2.15)$$

where ρ is the density of the liquid, v_0 and W are, respectively, the pre-exponential factor and the activation energy for carrier mobility. His computed results based on Equation (2.15), as shown in Table 2.3, agree well with experimental results of Crowe et al. [1954] for saturated hydrocarbons and of Sharbaugh et al. [1956] for aromatic hydrocarbons.

Another bubble theory for breakdown of dielectric liquids has been developed by Krasucki [1966]. He analyzed the development of a vapor bubble at high fields based on his observations in a high viscosity liquid as described in Section 2.3. However, his theory is similar to Kao's early theory [1965] except that Krasucki takes into account the change in the volume of the bubble.

The theories based on the bubble formation process not only can explain the dependence of breakdown strength on hydrostatic pressure but also can explain its dependence on molecular structure. Furthermore, the results of prebreakdown phenomena described in Section 2.3 provide also a strong support of this breakdown process. However, there is still no experimental results to show directly the mechanisms responsible for the formation of such micro-bubbles in dielectric liquids.

Table 2.3 Comparison of theory with experiment [after Kao 1976].

TABLE I
BREAKDOWN STRENGTHS OF SATURATED HYDROCARBON LIQUIDS

LIQUID	STRUCTURE	MOLECULAR WEIGHT	DENSITY g/cm ³	BOILING POINT °C	SPECIFIC HEAT Cal/R-°C	RELATIVE PERMITTIVITY	BREAKDOWN STRENGTH ^{II} kV/cm	
							EXPERIMENTAL*	THEORETICAL
n-Hexane C ₆ H ₁₄	Straight chain	86.17	0.659	68.70	0.5440	1.890	1.56	1.56
2-Methyl-pentane	One branch	86.17	0.654	60.20	0.5325	1.881	1.49	1.47
2,3-Dimethyl-butane	Two branches	86.17	0.662	57.98	0.5245	1.890	1.38	1.46
2,2-Dimethyl-butane	Two branches	86.17	0.649	49.70	0.5215	1.873	1.33	1.35
n-Heptane C ₇ H ₁₆	Straight chain	100.20	0.684	98.40	0.4900	1.920	1.66	1.67
2,4-Dimethyl-pentane	Two branches	100.20	0.673	80.50	0.5290	1.914	1.44	1.48
n-Octane C ₈ H ₁₈	Straight chain	114.22	0.703	125.50	0.5780	1.948	1.79	1.86
2,2,4-Tri-methyl-pentane	Three branches	114.22	0.692	99.20	0.4890	1.940	1.40	1.47
n-Decane C ₁₀ H ₂₂	Straight chain	142.27	0.730	174.10	0.5280	1.991	1.92	1.91

* The experimental breakdown strengths of the liquids are taken from the paper of Crowe, Sharbaugh and Bragg (1954). Gap length: $d = 0.051$ mm and pulse duration: $\tau = 1.4$ μ s.

TABLE II
BREAKDOWN STRENGTHS OF AROMATIC HYDROCARBON LIQUIDS

LIQUID	STRUCTURE	MOLECULAR WEIGHT	DENSITY g/cm ³	BOILING POINT °C	SPECIFIC HEAT Cal/g-°C	RELATIVE PERMITTIVITY	BREAKDOWN STRENGTH ^{II} kV/cm	
							EXPERIMENTAL*	THEORETICAL
Benzene C ₆ H ₆		78.11	0.879	80.08	0.4060	2.284	1.63	1.94
Methyl-benzene C ₆ H ₅ -CH ₃		92.13	0.866	110.60	0.4000	2.379	1.99	2.15
Ethyl-benzene C ₆ H ₅ -C ₂ H ₅		106.16	0.867	136.15	0.4164	2.412	2.26	2.27
n-Propyl-benzene C ₆ H ₅ -n-C ₃ H ₇		120.18	0.862	159.31	0.4240	2.373	2.50	2.30
1-Propyl-benzene C ₆ H ₅ -CH(CH ₃) ₂		120.18	0.864	152.42	0.4640	2.384	2.38	2.20
n-Butyl-benzene C ₆ H ₅ -n-C ₄ H ₉		134.21	0.862	183.10	0.4340	2.359	2.75	2.50
t-Butyl-benzene C ₆ H ₅ -t-C ₄ H ₉		134.21	0.867	168.70	0.4240	2.366	2.22	2.35

* The experimental breakdown strengths of the liquids are taken from the paper of Sharbaugh, Crewe and Cox (1956). Gap length: $d = 0.051$ mm and pulse duration: $\tau = 1.65$ μ s.

CHAPTER 3

THE OPTICAL MEASURING SYSTEMS

In this chapter, we shall describe in detail the optical measuring system used for the investigation of electric field distributions and prebreakdown phenomena to be presented in Chapters 4 - 6. Our system is mainly based on the Schlieren optical method and the shadowgraphic method, and therefore the principles, sensitivities and limitations of these two methods will be fully discussed. The experimental techniques involved in a particular investigation will be discussed separately in Chapters 4 - 6.

3.1 The Schlieren Optical Method

The Schlieren optical method has been used extensively for investigating density gradients in optically transparent media [Shapiro 1953, Holder and North 1963]. The density gradients which are sometimes called streaks can be converted to the Schlieren images because of the unequal refraction due to the unequal density from point-to-point in the region concerned. This method enhances the contrast and hence enables the observation of an extremely small change in density.

In fact this method has been known for more than 100 years and widely used in the fields of aerodynamics, hydrodynamics, optics and so on [Shapiro 1953, Holder and North 1963]. Regarding the applications of this method for studying dielectric phenomena, Ostromov has used this method to observe the electrohydrodynamic motion, and Hakim and Higham [1961] and Farazmand [1961] have used this method for studying



prebreakdown phenomena in n-hexane and other dielectric liquids.

3.1.1 The Basic Principle of the Schlieren Optical Method

The basic Schlieren optical system is shown in Fig. 3.1. L.S. is a high intensity light source which may be a laser or a high pressure mercury lamp. The output light beam from the source is brought to a parallel beam of the size sufficiently large to cover the test region by a condenser lens C_1 , a pin-hole H, and a collimating lens C_2 . A slit S controls the size of the beam entering the test region. A convex lens (or called "Schlieren lens") F converges the light beam from the test region in the focal plane where a knife edge is located before it forms the image of the test region onto a screen. In this system, if the refractive index is uniformly distributed in the test region, the initial parallel beam will be converged at the focal point P of lens F. If some disturbance causes a change in refractive index distribution in the test region, light will be refracted and this deflected light beam will no longer meet at P, but at a particular point Q with a deflecting distance δ from P. It should be noted that the beam bending downward means that the refractive index decreases with y; and the beam bending upward means that the refractive index increases with y. Thus the light which can pass through the focal plane can be discriminated by the position of the knife edge, and therefore the illumination brightness of the image on the screen is changed with this discrimination. For the observation of transient disturbances, the knife edge is generally so adjusted that the initial light can partially pass through the focal plane to provide a

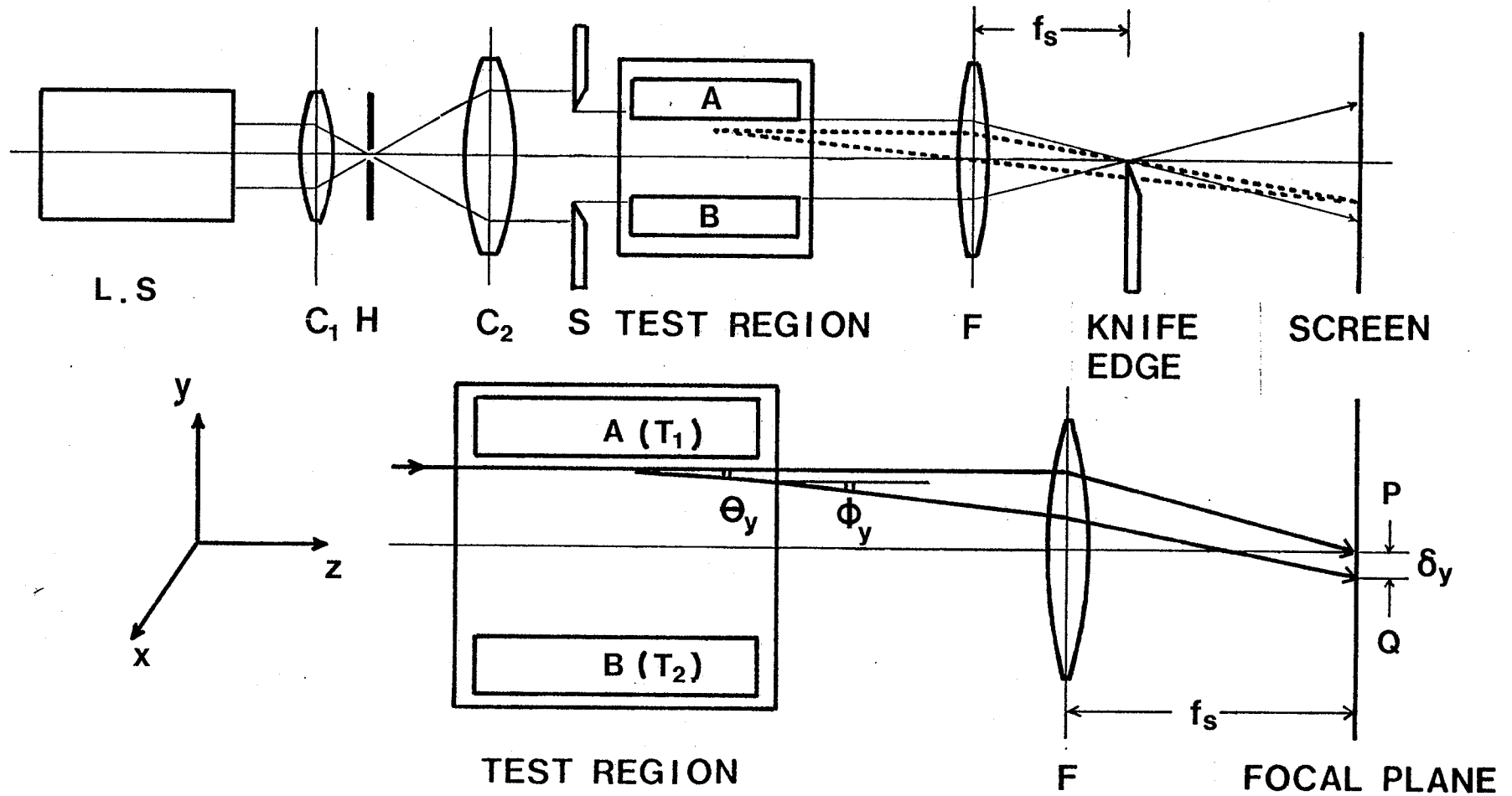


Fig. 3.1 The basic Schlieren system. L.S : light source; C_1 : condenser lens; H: pin-hole; C_2 : collimating lens; S: slit to control the size of the light beam entering the test region; F: Schlieren lens; f_s : focal length of lens F.

background image on the screen. In this case, the disturbances can be observed as bright and/or dark regions.

As has been mentioned above, the knife edge acts as a spatial filter, and therefore the Schlieren images on the screen can be changed by adjusting its position. For example, the bright regions and the dark regions of a Schlieren image will be reversed, if the knife edge is located on the opposite side of P to block the light through P rather than to block the light through Q. For some situations the knife edge filter is not suitable, particularly for time-varying events such as pre-breakdown and breakdown phenomena. Thus some investigators have used a black point dotted on a glass plate instead of the knife edge [Murooka and Sueda 1976]. This black point generally called the ring edge is located on the focal point P to block the non-deflected light and to allow all the deflected light relevant to the disturbance under investigation to pass through the focal plane. Therefore the disturbance can be clearly observed as a bright image in a dark background as the photographs shown in Fig. 2.5(b). This technique is useful when recording a time varying event (a disturbance or a phenomenon) by means of a high speed camera which generally requires a high intensity and high contrast light relevant to the phenomenon.

For the optical observation of a fast time-varying event, a high speed camera or a high speed photographic technique is commonly used. The early investigators, in general, used an ordinary mechanical high speed camera or a flash lamp with the time resolution of the order of a few milliseconds to a microsecond [Hakim and Higham 1961, Farazmand 1961]. In the recent years, accompanied with the development of laser

techniques, the time resolution has reached the level of the order of microseconds to nanoseconds [Marikawa 1972, Forster and Wong 1977]. It is important to note that the resolution of an optical method is sometimes limited by the high speed photographic technique.

In the following, we shall analyse in more detail the light beam passing through the test region as shown in Fig. 3.1. The light beam is refracted in an optically transparent medium by the refractive index gradients perpendicular to the parallel light beam. Since the parallel light beam is in the z-direction, the refracted light will form a refracted angle in the x-z plane and a refracted angle in the y-z plane. If the refractive index gradients are small, then according to the analysis of Wolin [1953], the total refracted angles which the light beam bends in the z-direction due to the refractive index gradients in the test region can be expressed as,

$$\theta_x = \frac{1}{n_0} \int_0^L \frac{\partial n(x,y,z)}{\partial x} dz \quad (3.1)$$

$$\theta_y = \frac{1}{n_0} \int_0^L \frac{\partial n(x,y,z)}{\partial y} dz \quad (3.2)$$

with second-order terms ignored, where θ_x and θ_y are, respectively, refracted angles in the x-z and y-z planes, n_0 is the average refractive index of the medium in the test region, $n(x,y,z)$ is the refractive index, and the region from $z = 0$ to $z = L$ is the test region. From Fig. 3.1 it can be easily shown that the deflecting distance δ is given by

$$\delta = f_s \phi \quad (3.3)$$

and

$$\phi = \frac{n_o}{n_a} \theta \quad (3.4)$$

where f_s is the focal length of lens F and n_a is the refractive index of the medium outside the test region. Substitution of Equation (3.4) into Equation (3.3) gives

$$\delta = \frac{n_o}{n_a} f_s \theta \quad (3.5)$$

Substitution of Equation (3.5) into Equations (3.1) and (3.2) gives

$$\delta_x = \frac{f_s}{n_a} \int_0^L \frac{\partial n(x,y,z)}{\partial x} dz \quad (3.6)$$

$$\delta_y = \frac{f_s}{n_a} \int_0^L \frac{\partial n(x,y,z)}{\partial y} dz \quad (3.7)$$

It can be seen from Equations (3.6) and (3.7) that the refractive index gradient can be determined by measuring the deflecting distances, δ_x and δ_y .

The resolution of this method is governed by the Rayleigh criterion [Kinbara 1964], which is given by

$$r = G \frac{f_s \lambda}{D} \quad (3.8)$$

where r is the size of the focal point image, D is the parallel beam width,

λ is the wavelength of the light, and G is a constant. Substitution of Equation (3.3) into (3.8) gives

$$\frac{\delta}{r} = \frac{1}{G} \frac{D\phi}{\lambda} \quad (3.9)$$

The higher the ratio of δ/r , the higher is the resolution of this method. Thus, for a high resolution we have to use (i) a light beam of short wavelength, but the medium under test must be transparent to it, (ii) a light beam with a very narrow linewidth, such as a highly coherent light from gas lasers, (iii) a large parallel beam width, and (iv) a high resolution photo-detector. For accurate measurements of the deflecting distance δ , the graded filter technique in place of the conventional knife edge method is recommended [Kent 1969]. However, for an actual Schlieren optical system; the sensitivity is also related to the divergence of the initial parallel beam, the perfectness of the lenses and their arrangements and so on. Thus the sensitivity of an actual system shall be described in the section 3.1.2.

3.1.2 The Schlieren Optical System used for Measurements of Field Distributions and other Disturbances

The Schlieren optical system is shown in Fig. 3.2. The light source was a He-Ne laser of 5 mw. The size and divergence of the parallel beam were, respectively, 25 mm in diameter and 1×10^{-3} rad in full angle. The lens F was a biconvex lens, and the diameter and the focal length of lens F were, respectively, 40 mm and 200 mm (or 500 mm). The knife edge was a stainless steel razor blade. This blade was located in parallel with the x-direction in the focal plane of lens F, and its position was adjusted along the y-direction using a driving screw and a dial-micro-gauge as

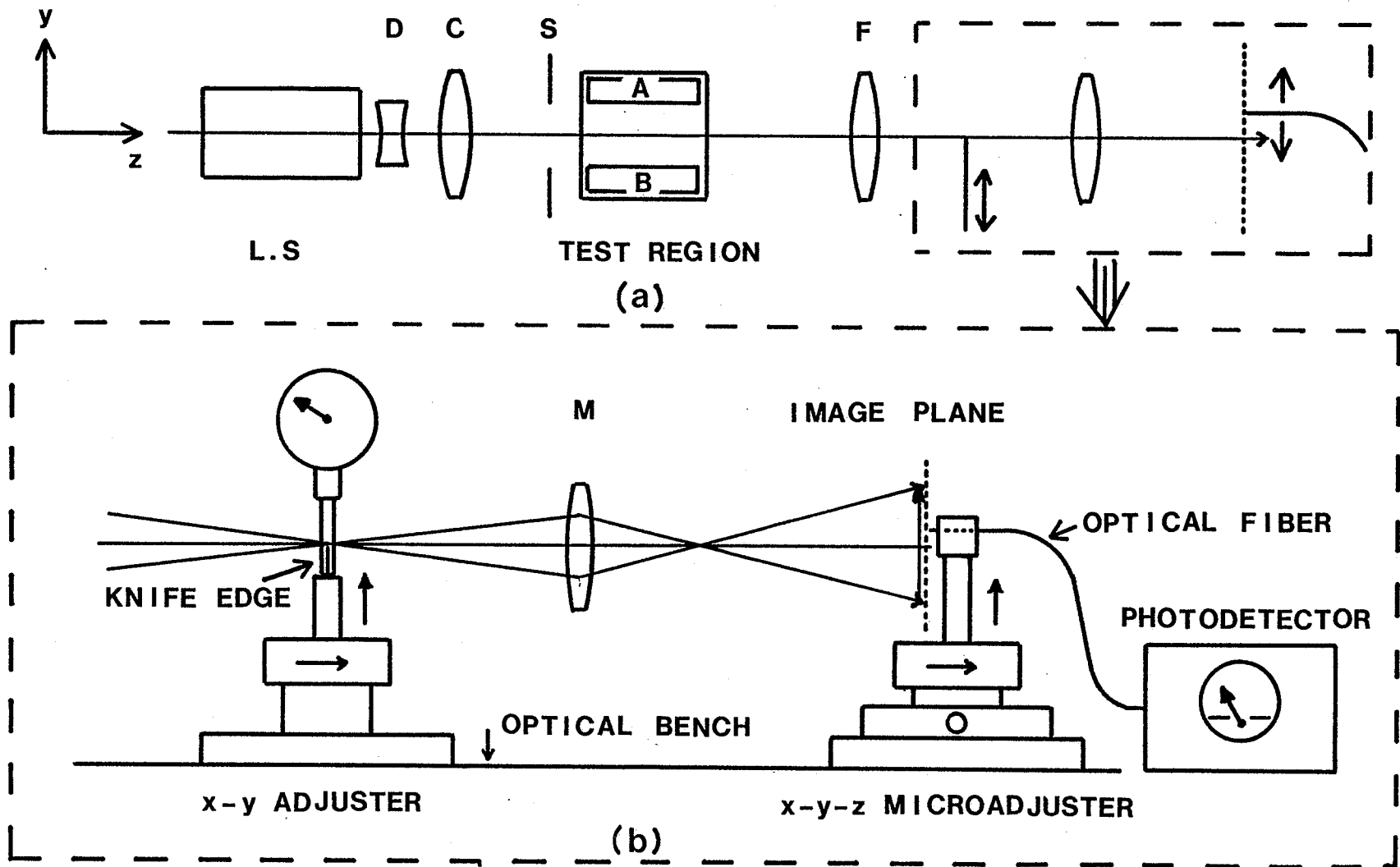


Fig. 3.2 The Schlieren system. L.S.: He-Ne laser (light source); D, diffusing lens; C, collimating lens; S, slit to control the size of the light beam entering the test region; F, Schlieren lens; M, magnifying lens.

shown in Fig. 3.2(b). This knife edge can be used to discriminate the deflecting distance δ_y , and therefore, according to Equation 3.7, the refractive index gradient for the y-direction can be determined. In this system, a biconvex lens was placed after the knife edge to control the magnification of the image of the test region on a screen. The screen was a white board and this was used for adjusting the focusing. For the determination of the position Q corresponding to a particular point in the test region, a tip of an optical fiber (0.12 mm in diameter) was used instead of the board, and located in the same place on the board. The position of this optical fiber tip was controlled in the x-y plane by using a two-dimensional micro adjuster as shown in Fig. 3.2(b). The other end of the optical fiber was connected to a high sensitivity photomultiplier.

Typical results for the image illumination brightness on the screen as a function of the position of the knife edge is shown in Fig. 3.3. This curve was obtained under the following conditions; the diameter of the parallel beam was 12 mm, the focal length of lens F was 500 mm, the brightness without the knife edge was adjusted to be 100% when the tip of the optical fiber was located at the center of the image. From this figure it can be seen that, with slightly masking, the illumination brightness can exceed 100% due to diffraction of the light by the knife edge. The maximum change in illumination brightness is 4.3%/1 μ m which occurs around the point corresponding to the 50% of the difference between the maximum and minimum brightness as the location of the knife edge moved along the y direction.

The accuracy of our photodetector was estimated to be about 97% and therefore we took a brightness change of 3% as the detectable brightness

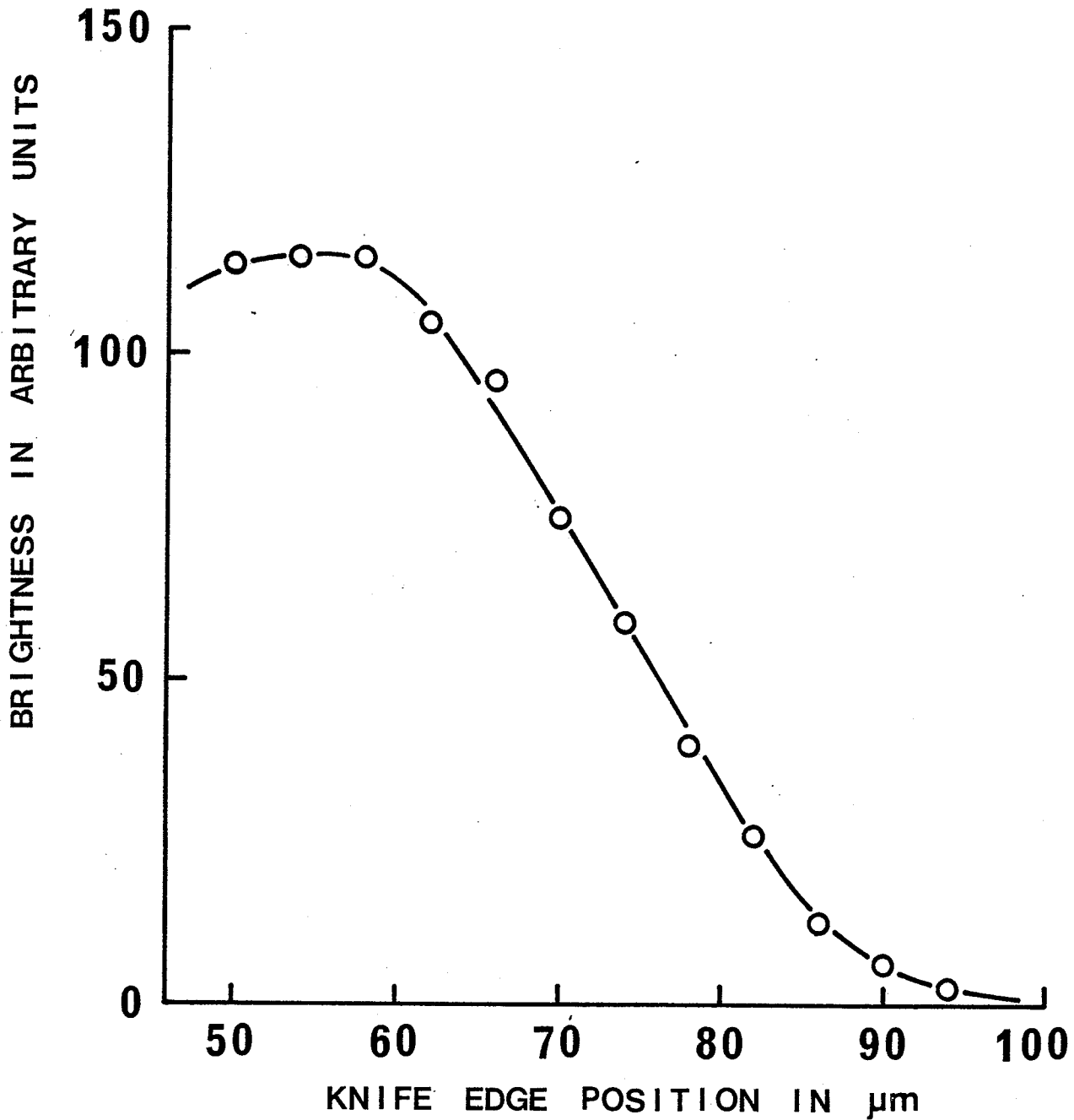


Fig. 3.3 Typical variation of the image brightness on the screen with the knife edge position along the v-direction (with respect to an arbitrary reference position).

change. Thus the detectable deflecting distance is ($3/4.3 = 0.7\mu\text{m}$), which corresponds to conditions of $f_s = 500$ mm and $D = 12$ mm. This means also that, according to Equation (3.3), the detectable deflecting angle ϕ_d is $(0.7 \times 10^{-3}/500) = 1.4 \times 10^{-6}$ rad. The detectable refracted angle ϕ_d as a function of the diameter of the parallel beam is shown in Fig. 3.4. The curve (a) and the curve (b) are, respectively, for lens F having a focal length of 200 mm and 500 mm. Obviously, the detectable refracted angle ϕ_d decreases with increasing diameter D , and the relation between ϕ_d and D in mm can thus be written as

$$\phi_d = \frac{14}{D} \times 10^{-6} \text{ rad} \quad (3.10)$$

with the conditions that f_s is from 200 mm to 500 mm, and D is smaller than 10 mm. Equation (3.10) gives the minimum sensitivity for our Schlieren optical system. The minimum sensitivity was almost independent of the focal length f_s under the above conditions. However, for a short focal or a large parallel beam width, the sensitivity tends to reach a saturation by the dispersion due to the knife edge as shown in Fig. 3.4.

For the measurement of the deflecting distance δ , we chose the point corresponding to 50% of the difference between the maximum and minimum brightness as the location of P and Q in the y-direction. Because, our system has the highest sensitivity around that point. However, the illumination brightness near the solid surface having a long distance along the x-direction is affected by the diffraction due to the surface as shown in Fig. 3.5. Thus, when we measured the deflecting distance near the solid surface, we chose the point corresponding to the 25% instead of 50%.

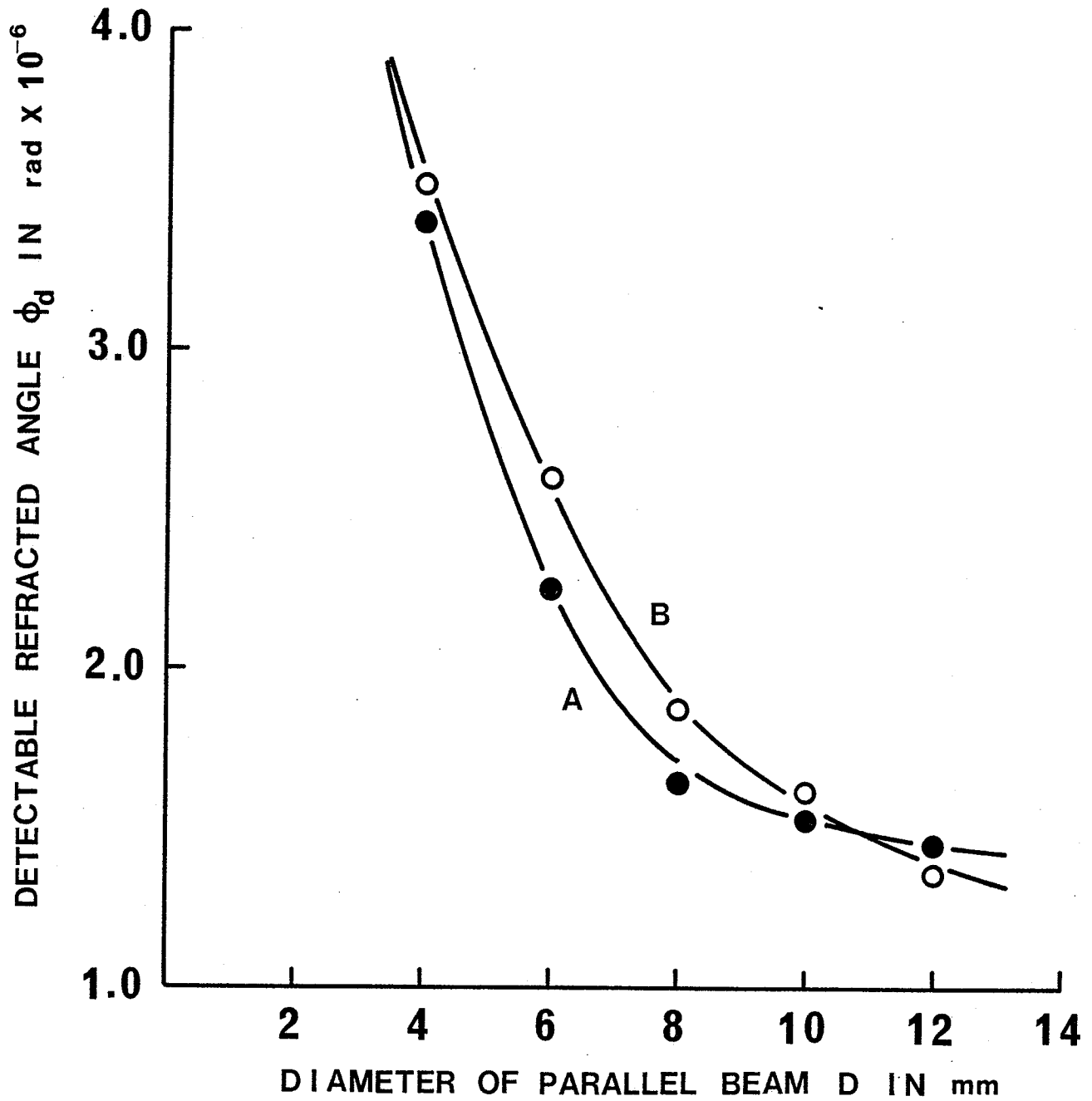


Fig. 3.4 The detectable refracted angle ϕ_d as a function of the diameter of the parallel beam. A: $f_s = 200$ mm; B: $f_s = 500$ mm.

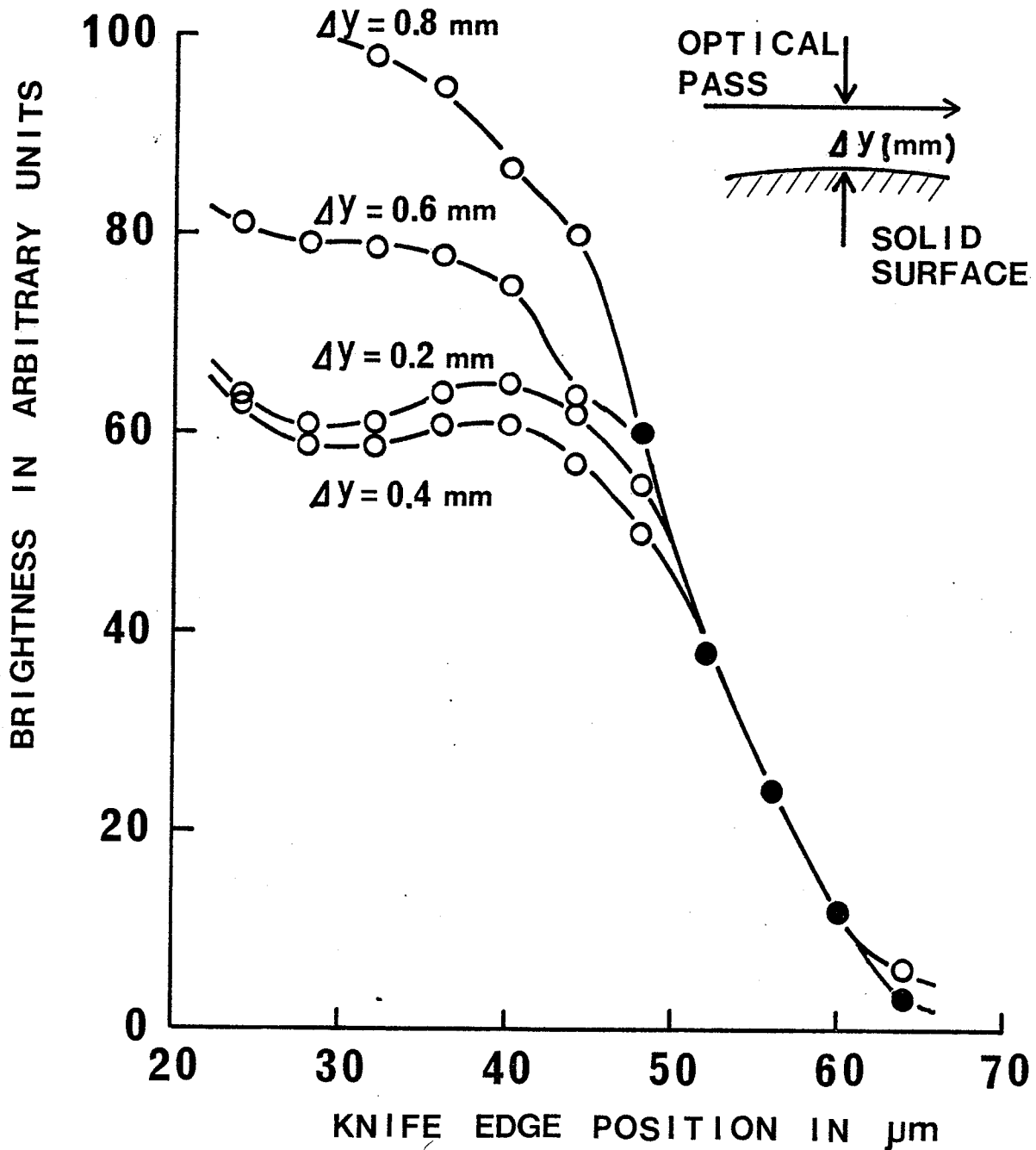


Fig. 3.5 Typical variation of the image brightness on the screen for the light passing through near the solid surface with the knife edge position along the y -direction (with respect to an arbitrary reference position).

between the maximum and minimum brightness to determine the location of P and Q in the y-direction to take into account such an influence. In the next section, we shall show the use of our system for the measurements of temperature gradients in terms of refractive index gradients.

3.1.3 The Measurements of Temperature Gradients

The temperature distribution in dielectric liquids is generally measured by means of thermocouples. This conventional method has the following disadvantages; (i) the thermocouples placed near the test region may disturb the original condition of the region, and hence the measured temperature distribution may not represent the real one inside the region, and (ii) the inertia of the thermocouple measurements precludes the study under rapid transient conditions. Several investigators made use of the principle of Schlieren interferometry for the measurements of temperature distributions in air and liquids [Reisman and Sutton 1965, Brackenridge and Gilbert 1965], but this technique has not been fully discussed from the view point of practical applications. Therefore, in this section, we describe the principle and the resolution of the Schlieren method for temperature distribution measurements and other applications.

(A) Theory

It is well known that the refractive index changes with temperature because of the temperature dependence of the material density. If the change in temperature is small and the temperature distribution is stable, the refractive index $n(x,y,z)$ as a function of temperature $T(x,y,z)$ in the steady state may be written as

$$n(x,y,z) = n_0 + k_n [T(x,y,z) - T_0] \quad (3.11)$$

where n_0 and k_n are, respectively, the refractive index and the temperature coefficient of the refractive index of the material corresponding to the average temperature T_0 . If the refracted angle θ caused by the change in temperature distribution is so small that we may use $\tan \theta \approx \theta$, substitution of Equation (3.11) into Equations (3.6) and (3.7) yields

$$\delta_x = \frac{k_n f_s}{n_a} \int_0^L \frac{\partial T(x,y,z)}{\partial x} dz \quad (3.12)$$

$$\delta_y = \frac{k_n f_s}{n_a} \int_0^L \frac{\partial T(x,y,z)}{\partial y} dz \quad (3.13)$$

Thus, the average temperature gradient in the test region along the x-direction at any value of y and that along the y-direction at any value of x may be written, respectively, as

$$\frac{d\bar{T}}{dx} = \frac{n_a}{k_n f_s} \delta_x \quad (3.14)$$

$$\frac{d\bar{T}}{dy} = \frac{n_a}{k_n f_s} \delta_y \quad (3.15)$$

On the basis of these two equations, the average temperature gradient at any point in the test region in the x-y plane can be determined by measuring δ_x and δ_y corresponding to this particular point.

(B) Experimental

In our simple experiment, the glass cell with two optically-flat

windows on both sides facing the z-direction was used as the container of a dielectric liquid which was benzene or n-hexane for the present investigation. The temperature difference $T_1 - T_2$ was applied to the aluminum plates A and B as shown in Fig. 3.1 and was maintained constant by a thermostatically controlled heat source. In order to produce a constant temperature gradient in the liquid between the two plates, the size of the plates was made about the same size of the test cell and their separation was kept as small as possible. Before the application of the temperature difference $T_1 - T_2$ the temperature in the liquid is assumed to be uniformly distributed with the temperature gradient equal to zero. The parallel beam passing through the test cell in the z-direction will meet at point P in the focal plane. After the application of the temperature difference $T_1 - T_2$, the refractive index tends to decrease from plate B at a lower temperature towards plate A at a higher temperature. In this case, the light beam will be deflected at a refracted angle θ_y , with respect to the z-direction in the test region as shown in Fig. 3.1. This deflected beam will meet at Q in the focal plane with a distance of δ_y below P. To measure the average temperature $\overline{dT/dy}$ at any point in the x-y plane in the test region, we located the photo-detector at the same point in the image on the screen as described section 3.1.2 and adjusted the position of the knife edge to determine this particular point Q. By measuring the distance δ_y between P and Q, we can determine $\overline{dT/dy}$ using Equation (3.15). With this method we can determine $\overline{dT/dy}$ and $\overline{dT/dx}$ at any point in the test region. Typical results plotted in δ_y as a function of temperature difference $T_1 - T_2$ for benzene and n-hexane are shown in Fig. 3.6 in which the value of δ_y is the average value of δ_y measured at four different points along the y direction

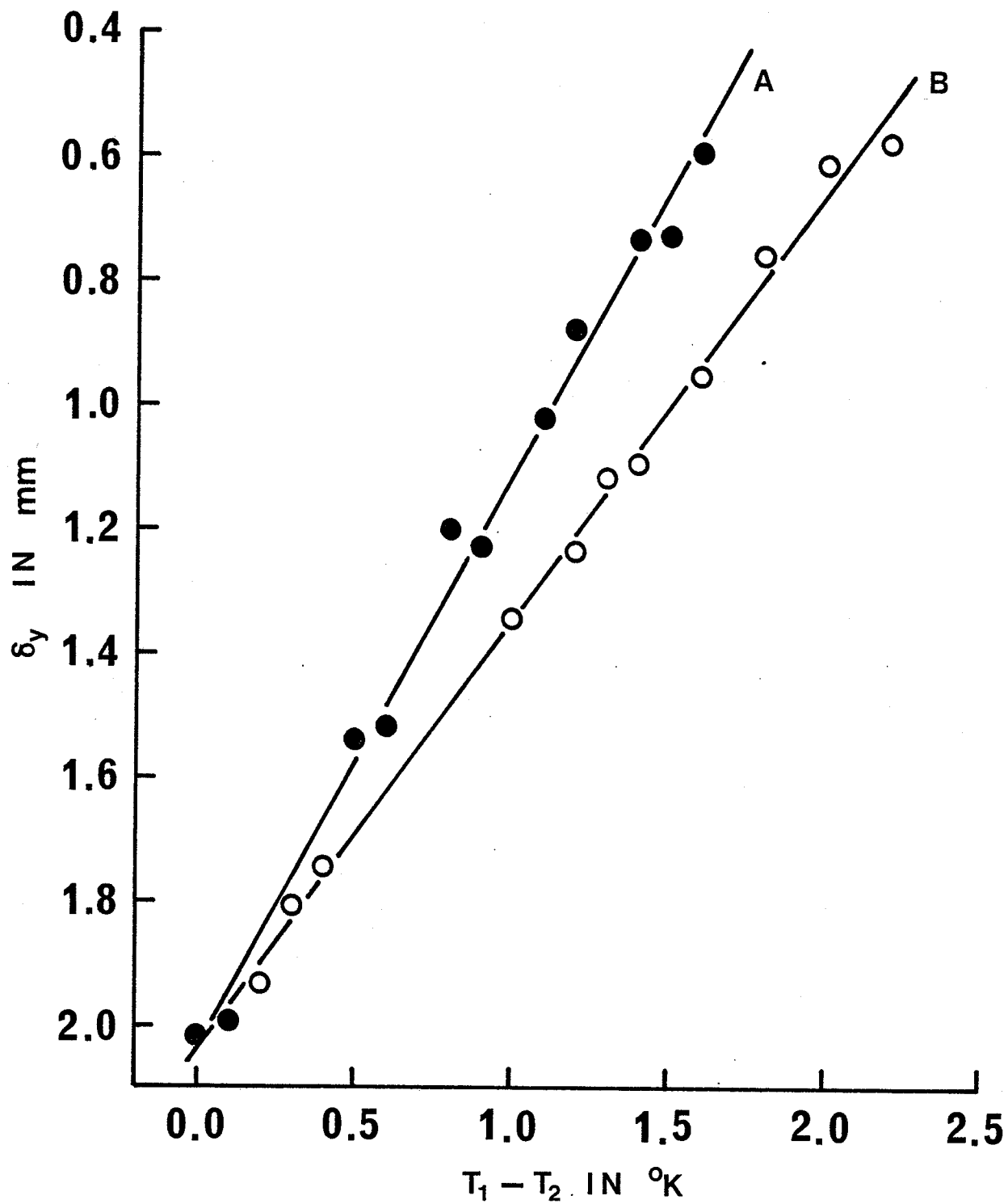


Fig. 3.6 δ_y as a function of temperature difference $T_1 - T_2$ for (A) benzene and (B) n-hexane (with respect to an arbitrary reference position).

between plates A and B. It should be noted that the values of δ_y for the four different points were very close to each other because for a fixed temperature difference $T_1 - T_2$, $\overline{dT/dy}$ was found practically constant along the y-direction as expected for the experimental arrangement shown in Fig.3.1. δ_y increases linearly with increasing temperature difference between the plates indicating that the experimental results are in good agreement with Equation (3.15).

(C) Discussion

To further examine the correlation between the experiment and the theory, we have calculated the values of K_n from Equation (3.15) and the experimental data, and compared them with the accepted values available in the literature. In analogy to a parallel plate condenser, there is a fringing effect between plates A and B in Fig. 3.1. Thus the effective length of the test region L is not the length of the plate ℓ along the z-direction, but smaller than ℓ to take into account this fringing effect. By a rough approximation we can use the following relation to estimate L

$$L = \ell - d \quad (3.16)$$

where d is the separation between the two plates. Using the data in Fig. 3.6 and $f = 20$ cm, $\ell = 4$ cm, $d = 0.5$ cm and $n_a = 1$ (in air) for our experiments, we have calculated the values of K_n for benzene and n-hexane, which are $6 \times 10^{-4} \text{ }^\circ\text{K}^{-1}$ and $5 \times 10^{-4} \text{ }^\circ\text{K}^{-1}$, respectively for the temperature range of $18^\circ\text{C} - 22^\circ\text{C}$ used. These values are in reasonable agreement with the published values of $6.31 \times 10^{-4} \text{ }^\circ\text{K}^{-1}$ for benzene and $4.89 \times 10^{-4} \text{ }^\circ\text{K}^{-1}$ for n-hexane for about the same temperature range [Timmermans p. 147]. To

avoid calculating L , we can also, according to Equation (3.15), compare the ratio

$$\frac{k_n(\text{n-hexane})}{k_n(\text{benzene})} = \frac{\delta_y(\text{n-hexane})}{\delta_y(\text{benzene})} \quad (3.17)$$

for the same value of $\overline{dT/dy}$. From Fig. 3.6 this ratio is 0.7753 which agrees strikingly well with the ratio of 0.7749 based on the published values [Timmermans p. 147]. Thus with a standard sample as reference the values of k_n and thermal conductivities of any materials can be determined accurately by this method. In our simple arrangement shown in Fig. 3.2, we can measure accurately temperature gradients as small as 2×10^{-3} deg/cm which cannot be detected by the conventional method.

It should be noted that the above results used to demonstrate the principle provide only the average values of $\overline{dT/dy}$ (average along the z -direction) in the x - y plane. In general, dT/dy varies with z . To determine the actual temperature at any point (x, y, z) , we have to obtain the actual value of dT/dy at that particular point. To do this, we have to adjust the direction of the parallel light beam to obtain more data of $\overline{dT/dy}$, the average value along the new directions which form an angle θ with the original z -axis. By varying θ , we can obtain as many values of $\overline{dT/dy}$ as required to determine the actual dT/dy at any point along the z -direction in the test region. Obviously, such calculations are tedious but can be easily done by the computer.

In principle, the Schlieren method can be used to determine the temperature distributions for any dielectric systems of any configurations;

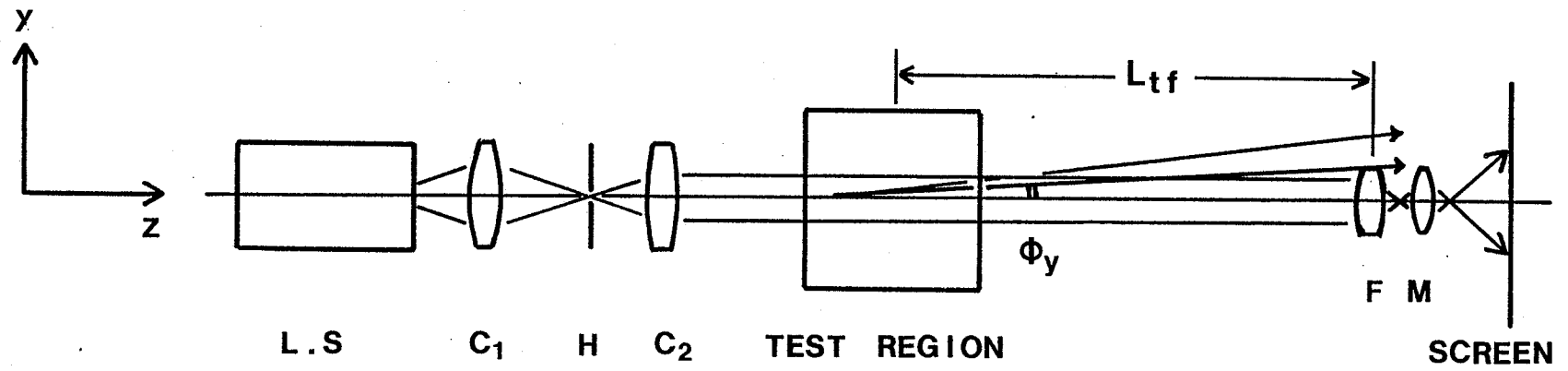
and can also be used to measure the thermal conductivity of any material of any geometric shape, and to study the temporal change of temperature distributions under rapid transient conditions because of the fast response inherent in this optical technique.

3.2 The Shadowgraphic Method

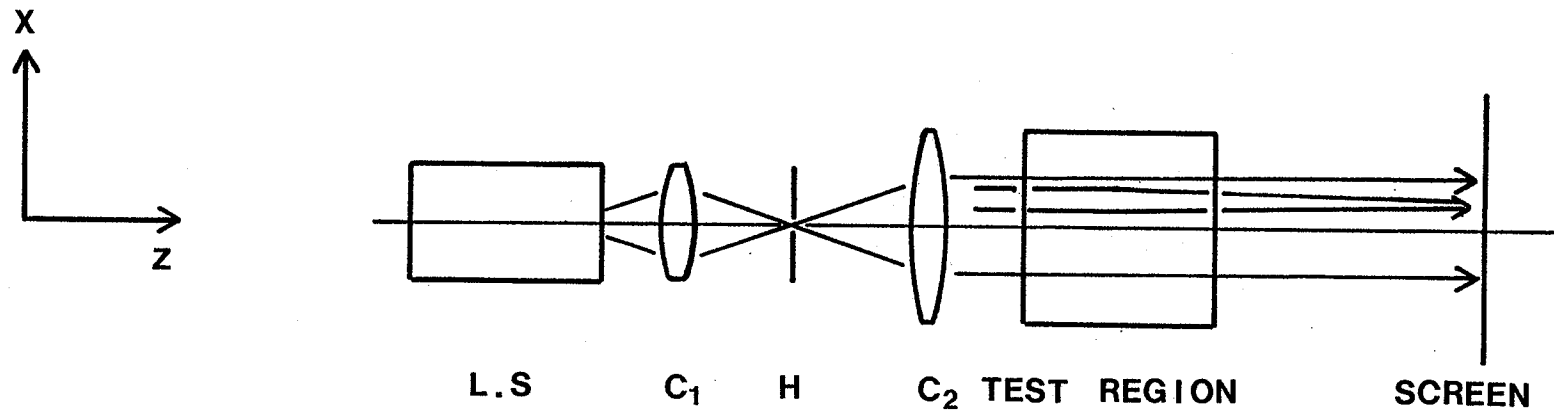
As well known as the Schlieren optical method, the shadowgraphic method has long been used for the studies of prebreakdown and breakdown phenomena by the refracted light due to the refractive index gradient. This method is mainly used for detecting the disturbances accompanied with a large refractive index change.

3.2.1 The Basic Difference Between the Shadowgraphic Method and the Schlieren Optical Method

The optical system for the shadowgraphic method can be considered to be the same as the basic Schlieren optical system with the knife edge removed as shown in Fig. 3.7(a). In this system, the light beam passing through lens F will form an image of any disturbance in the test region. However, if the initial light beam were largely refracted by some disturbance in the test region, the deflected light would no longer be able to pass through lens F, and therefore the missing light would form the dark regions corresponding to the disturbance on the screen. For the Schlieren optical method, the light which can pass through lens F is discriminated by means of the knife edge, while for the shadowgraphic method, the deflected light is discriminated by means of the location and the size of lens F.



(a)



(b)

Fig. 3.7 Shadowgraphic system. L.S.: light source; C₁: condenser lens; H: pin-hole; C₂: collimating lens; F: focusing lens; M: magnifying lens.

According to the principle of this method, the refracted angle ϕ corresponding to the dark regions can be written as

$$\phi > \frac{R}{L_{tf}} \quad (3.18)$$

where L_{tf} is the distance from the test region to lens F, and R is the radius of the lens. Thus, the sensitivity of the system can be easily controlled by changing the location and the size of lens F. The longer the distance and/or the smaller the size of lens, the higher is the sensitivity for the formation of the dark region. The controllable sensitivity is the advantage of this method, and therefore with this method the effects due to the subsequent disturbances created by the disturbance under investigation, or due to initial nonuniformity of the refractive index distribution in the test cell can be avoided. For example, breakdown phenomena are, in general, accompanied with a strong light emission which would disturb the observations of the breakdown process. In this case, the effect due to the emitted light can be avoided by adjusting the system to give the low sensitivity for the light [Takuma 1972].

In fact, the change of the refractive index distribution can be observed without lens F as shown in Fig. 3.7(b). This technique is also called the shadowgraphic method, and this method has been used in the field of aerodynamics. Although this method is based on the refraction of the light due to refractive index gradients, it depends on the second derivative rather than the first derivative of refractive index distributions, because, if the refractive index gradient were constant, the initial parallel beam would be deflected by the same amount, and there would be no change in

illumination brightness on the screen. Only if there is a gradient of the refractive index which will have a tendency to converge or diverge the light, the brightness will be changed. This method is therefore suitable for the studies of the disturbances with rapidly varying refractive index gradients such as shock waves [Shapiro 1953].

3.2.2 The Shadowgraphic System used for the Studies of Prebreak-down Phenomena

The electro-optical system is shown in Fig. 3.8. The basic arrangements is the same as the Schlieren optical system shown in Fig. 3.3. The distance L_{tf} and the radius R of lens F can, respectively, be changed between 200 mm to 1500 mm and 50 mm to 5 mm. Therefore, the refracted angle ϕ of the light which can pass through the lens can be controlled in the range of 3.5×10^{-1} to 3.3×10^{-3} rad. The disturbances were recorded using a movie camera.

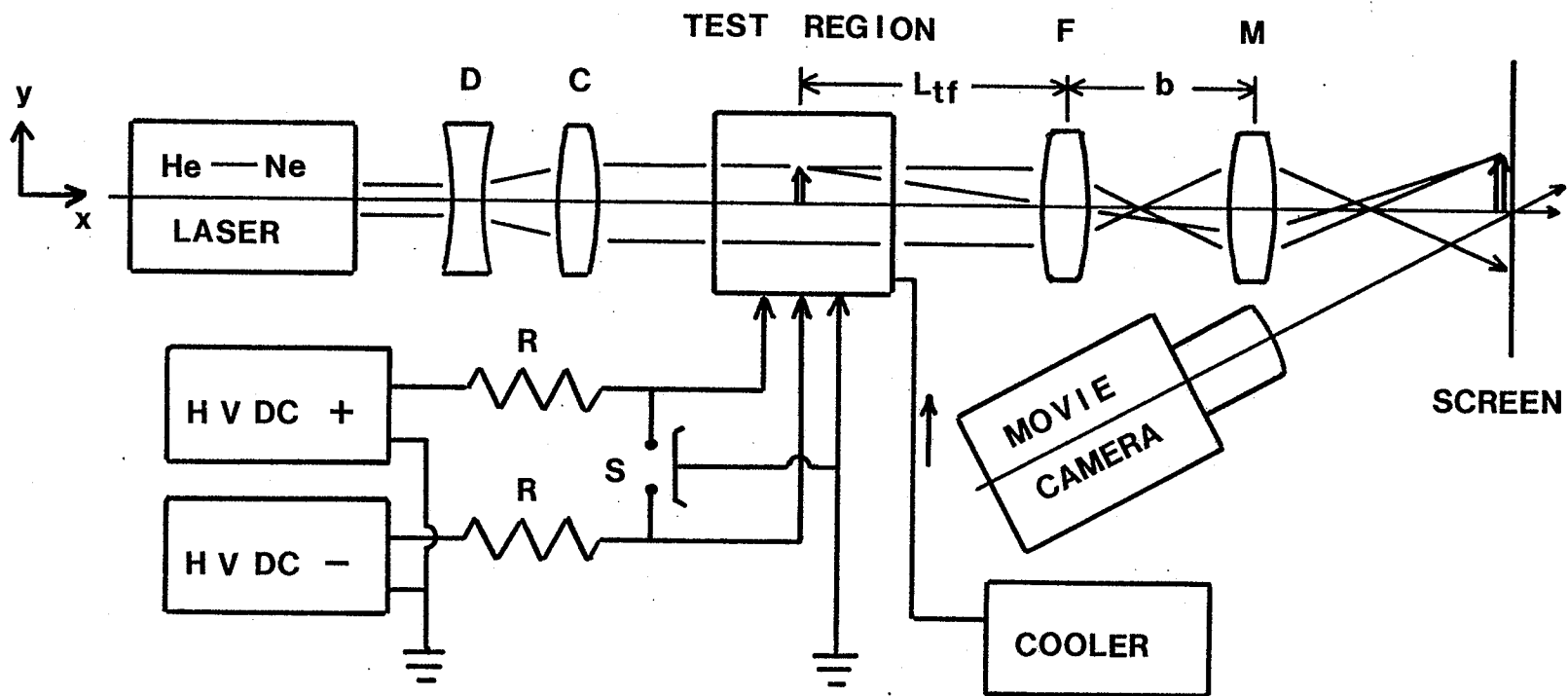


Fig. 3.8 Electro-optical system for the observation of prebreakdown phenomena. D: diffusing lens; C: collimating lens; F: focusing lens; M: magnifying lens.

CHAPTER 4

THE SCHLIEREN IMAGES

Spatial variation of the density of any optically transparent media can be converted to the Schlieren images because of the unequal refraction due to the unequal density from point to point in the region concerned. The Schlieren technique enhances the contrast and hence enables the observation of an extremely small change in density. If this technique is employed for studying the physical processes responsible for any disturbance in an electrically stressed dielectric liquid, the first question to be asked is: what are the factors resulting in a change of the refractive index? Apart from the breakdown phenomena and the plasma in which the refractive index depends also on the plasma oscillation; the most important factor causing a change in refractive index in any chemically stable dielectric is the change of its density, which may be produced either by temperature gradients or by pressure gradients or by both. The change in refractive index caused by other factors such as space charges alone (but not the action of space charges) are negligible. In this chapter we shall clarify the interpretation of the Schlieren images normally observed in electrically stressed dielectric liquids and demonstrate the importance of the effects of the already-existing temperature gradients in the test region, and of the difference in thermal conductivity between the electrodes and the dielectric medium.

4.1 Theory

There are always two important phenomena existing in an electrically

stressed dielectric liquid: One is the movement of charge particles (mainly ions) due to their interaction with the applied field resulting in matter transport or liquid motion, and the other is the interaction of spatial variation of the dielectric constant due mainly to the already-existing temperature gradient, with the applied field resulting also in liquid motion. Unless the temperature is perfectly controlled to maintain a constant temperature throughout the liquid, the electromechanical force is always present just because the random variation of temperature, though small, always exists from time to time and from domain to domain giving rise to a time-variant temperature gradient distribution. The Schlieren technique can detect only the phenomena which result from a spatial variation of the refractive index which is mainly caused by such an already-existing time-variant temperature gradient distribution in the liquid. The movement of ions itself should not introduce a change in refractive index if the ion concentration is not very large, but it would perturb the temperature gradient distribution and thus plays an indirect role in the formation of Schlieren images.

It can be imagined that a change in local temperature $T(x,y,z)$ at any point (x,y,z) will cause a change in density and hence a change in dielectric constant $\epsilon(x,y,z)$ and refractive index $n(x,y,z)$ at that point. Supposing that for a time interval Δt the temperature distribution is quasi-stable and the change of temperature at the point (x,y,z) as compared with the system average temperature is small, we can write for the time interval Δt

$$\epsilon(x,y,z) = \epsilon_0 + K_\epsilon [T(x,y,z) - T_0] \quad (4.1)$$

$$n(x,y,z) = n_0 + K_n [T(x,y,z) - T_0] \quad (4.2)$$

where ϵ_0 and n_0 are, respectively, the dielectric constant and the refractive index; and K_ϵ and K_n are their temperature coefficients of the material corresponding to the system average temperature T_0 .

According to the theory of electrodynamics, the interaction of the electric field $E(x,y,z)$ at any point with the spatial variation of the dielectric constant at that point will create an electromechanical forces in x,y, and z directions within an elementary volume $\Delta x \Delta y \Delta z$ tending to move the material within this elementary volume in such a direction to reduce the stored energy of the whole dielectric system. These forces can be expressed [Kao 1961] as

$$\Delta f_x = - DE^2 \frac{\partial \epsilon}{\partial x} \Delta x = - DK_\epsilon E^2 \frac{\partial T}{\partial x} \Delta x \quad (4.3)$$

$$\Delta f_y = - DE^2 \frac{\partial \epsilon}{\partial y} \Delta y = - DK_\epsilon E^2 \frac{\partial T}{\partial y} \Delta y \quad (4.4)$$

$$\Delta f_z = - DE^2 \frac{\partial \epsilon}{\partial z} \Delta z = - DK_\epsilon E^2 \frac{\partial T}{\partial z} \Delta z \quad (4.5)$$

where D is a constant. For dielectric liquids these forces tend to cause the liquid to move. The liquid motion which is generally referred to as the electrohydrodynamic phenomenon may be considered to be due mainly to two mechanisms: one is the Coulombic force resulting from the interaction of the space charge with the field, and the other is the electromechanical force resulting from the interaction of the spatial variation of the dielectric constant with the field. The direction of the former force depends on the types of ions (positively or negatively charged) and the direction of the field; while that of the latter is independent of the

direction of the field but depends on the temperature gradient. Thus the total forces causing the liquid motion can be written as

$$\Delta F_x = qNE_x \Delta x \Delta y \Delta z - DK_\epsilon E^2 \frac{\partial T}{\partial x} \Delta x \quad (4.6)$$

$$\Delta F_y = qNE_y \Delta x \Delta y \Delta z - DK_\epsilon E^2 \frac{\partial T}{\partial x} \Delta y \quad (4.7)$$

$$\Delta F_z = qNE_z \Delta x \Delta y \Delta z - DK_\epsilon E^2 \frac{\partial T}{\partial z} \Delta z \quad (4.8)$$

where N is the ion density of one type which may be positively charged or negatively charged at the point (x,y,z) , and q is the electron charge. There are some other effects which may also give rise to the motion of the liquid but these effects are not significant under normal conditions, and for simplicity they are not included in Equations (4.6) - (4.8).

For very pure liquids which contain a very low concentration of ionic impurities and at low applied fields in which no carrier injection from the electrodes and no carrier multiplication (such as ionization or dissociation) from the bulk are involved, the dominant mechanism for the liquid motion is the electromechanical force resulting from the already-existing local temperature gradient, that is the force given by Equations (4.3) - (4.5) or the second terms of Equations (4.6) - (4.8). If this is the case, the observed Schlieren images should correspond to the motion of the liquid from a region with a higher dielectric constant to a region with a lower dielectric constant. The direction of this motion is purely dependent on the temperature gradient distribution, and therefore the motion is quite random. The liquid propagation velocity, in this case,

should show a square law dependence of the applied voltage. For liquids containing a high concentration of ions, then the first terms of Equations (4.6) - (4.8) become dominant, and in this case the observed Schlieren images should still correspond to the temperature gradient distribution because only the temperature gradient would result in a significant spatial variation of both the dielectric constant and the refractive index. The liquid motion can be seen in the Schlieren images not because the ionic movement changes the spatial distribution of ion concentration but rather because the ionic movement modifies the original temperature gradient or induce a temperature gradient and hence it plays only an indirect role in the formation of Schlieren images. The concentration of homospace charge (one type of ions), because of mutual Coulombic repulsion, would never reach a value sufficiently high to cause a change in refractive index, and thus space charge itself should not produce Schlieren images.

For simplicity we shall confine ourselves to the discussion of the forces in the y -direction. The average temperature gradient as a function of the deflecting distance δ_y along the y direction is given by Equation (3.15). The average temperature gradient refers to its average over the length L . From Equations (4.7) and (3.15), δ_y is the measure of the average temperature gradient and hence the electromechanical force.

4.2 Experimental Techniques

To illustrate the effects of the already-existing temperature gradients on the Schlieren images, a simple electrode system shown in Fig. 4.1 was used in conjunction with the Schlieren system shown in Fig. 3.2. The glass test cell with two optically flat windows on both sides facing the

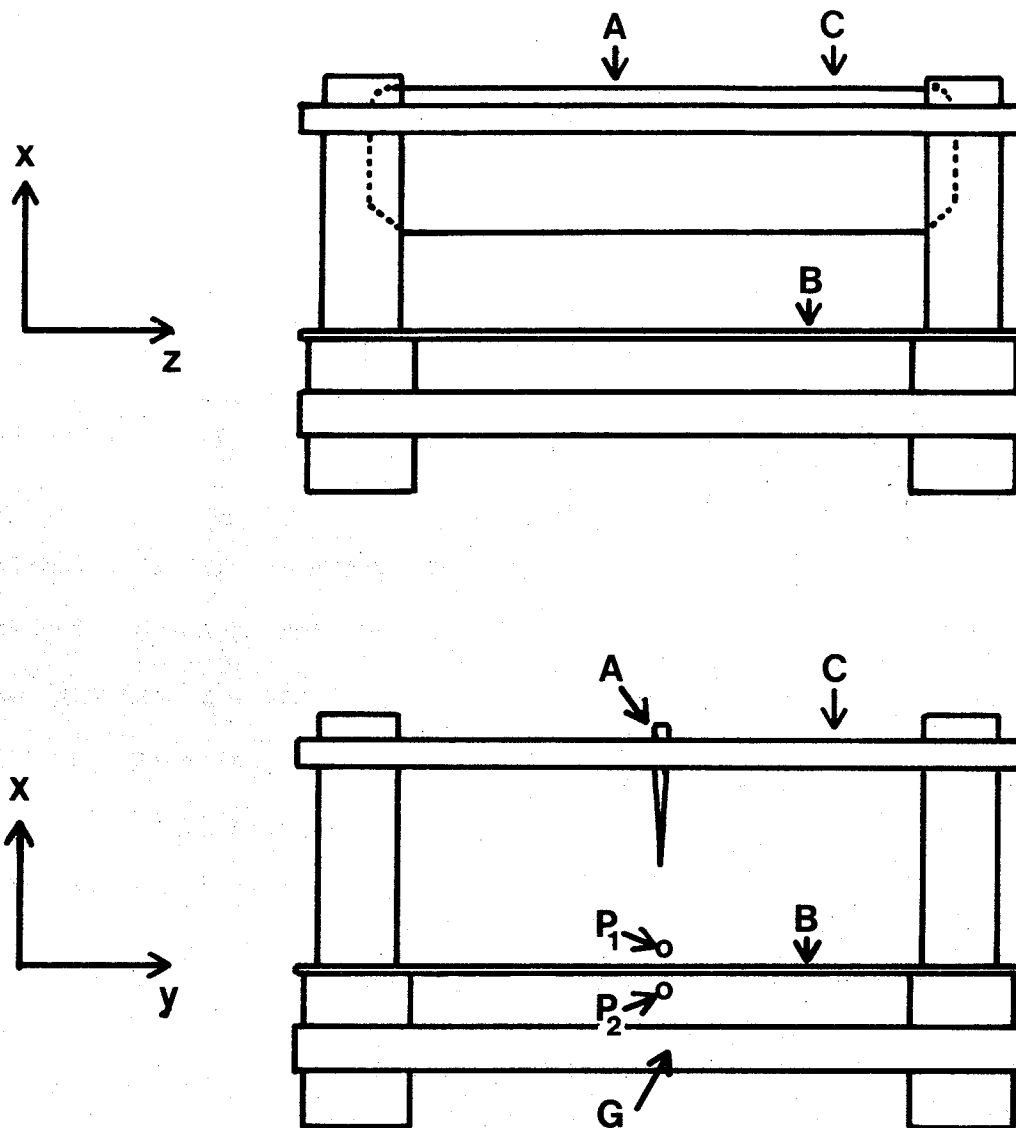


Fig. 4.1 The electrode system for the study of the Schlieren images in electrically stressed dielectric liquids. A, stainless steel blade; B, 0.2 mm thick copper plate; C, Teflon electrode supporting frame; P_1 and P_2 , measuring points of temperature gradients.

z-direction was used as the container of a dielectric liquid which was silicone oil for this investigation. A stainless steel blade of 36 mm in width and 6×10^{-3} mm in edge radius, and a copper plate of 47 mm x 47 mm x 0.2 mm were used as electrodes and they were held firmly with a separation of 6 mm by a framework made of teflon. A positive or a negative step-voltage pulse from a high-stability dc supply was applied to the blade electrode with the plate electrode connected to the neutral ground. As described in Section 3.1, by measuring the illumination brightness of the Schlieren image, it is possible to map the density or the refractive index distribution profile of the dielectric under any test conditions. We used the system and the technique described above for examining some phenomena in electrically stressed dielectric liquids, which are related to the Schlieren images and whose interpretations are still questionable.

4.3 Experimental Results and Discussion

The phenomenon of liquid motion has been studied by many investigators in the past two decades [Secker and Aplin 1970, Morant 1960, Filipini et al. 1970]. However, a clear interpretation of this phenomenon is still lacking. In view of this fact, we have attempted to look at this phenomenon from a different angle by examining the effect of the already-existing temperature gradient in the liquid. Silicone oil was chosen for this investigation. Before presenting the results, we would like to explain how an already-existing temperature gradient interacts with the ionic movement to create a resulting spatial variation of the refractive index which produces the observed Schlieren images on the screen. Supposing that in the liquid

between a blade and a plate electrodes the initial temperature increases linearly with y at $t = 0$ as shown in Fig. 4.2(a), and that at an appropriate applied field the liquid starts to move at $t = 0$ from the blade towards the plate due mainly to the ionic movement and the temperature gradient $(dT/dy)_0$, then the liquid motion will increase the temperature and hence the temperature gradient towards the plate because $(dT/dy)_0 > 0$. At $t = t_1$ a portion of the liquid originally located near the blade at $t = 0$ has moved to somewhere in the gap at $t = t_1$. By that time and at that position the temperature gradient increases from the original $(dT/dy)_0$ to $(dT/dy)_1 > (dT/dy)_0$. This implies that in this case the electromechanical force, according to Equation (4.4), tends to push the liquid towards the blade, in the direction just opposite to that of the ionic movement. The net force responsible for the liquid motion is therefore the difference between the Coulombic force experienced by the ions under an applied field and the electromechanical force. Since the former force is larger than the latter, the liquid moves from the blade towards the plate. At $t = t_2$ this portion of the liquid has moved to a position near the plate, which increases the temperature of the plate, and hence the temperature gradient at the position just below the plate becomes $(dT/dy)_2 > (dT/dy)_0$. However, if the initial temperature decreases linearly with y at $t = 0$ as shown in Fig. 4.2(b) with the ionic movement remaining in the same direction as for Fig. 4.2(a), in this case the ionic movement tends to lower the temperature towards the plate, thus at $t = t_1$, $(dT/dy)_1 < (dT/dy)_0$; and at $t = t_2$, $(dT/dy)_2 < (dT/dy)_0$. This implies that the electromechanical force is in the same direction as the Coulombic force experience by the ions. These two forces are additive, resulting in a more severe liquid motion for the case with

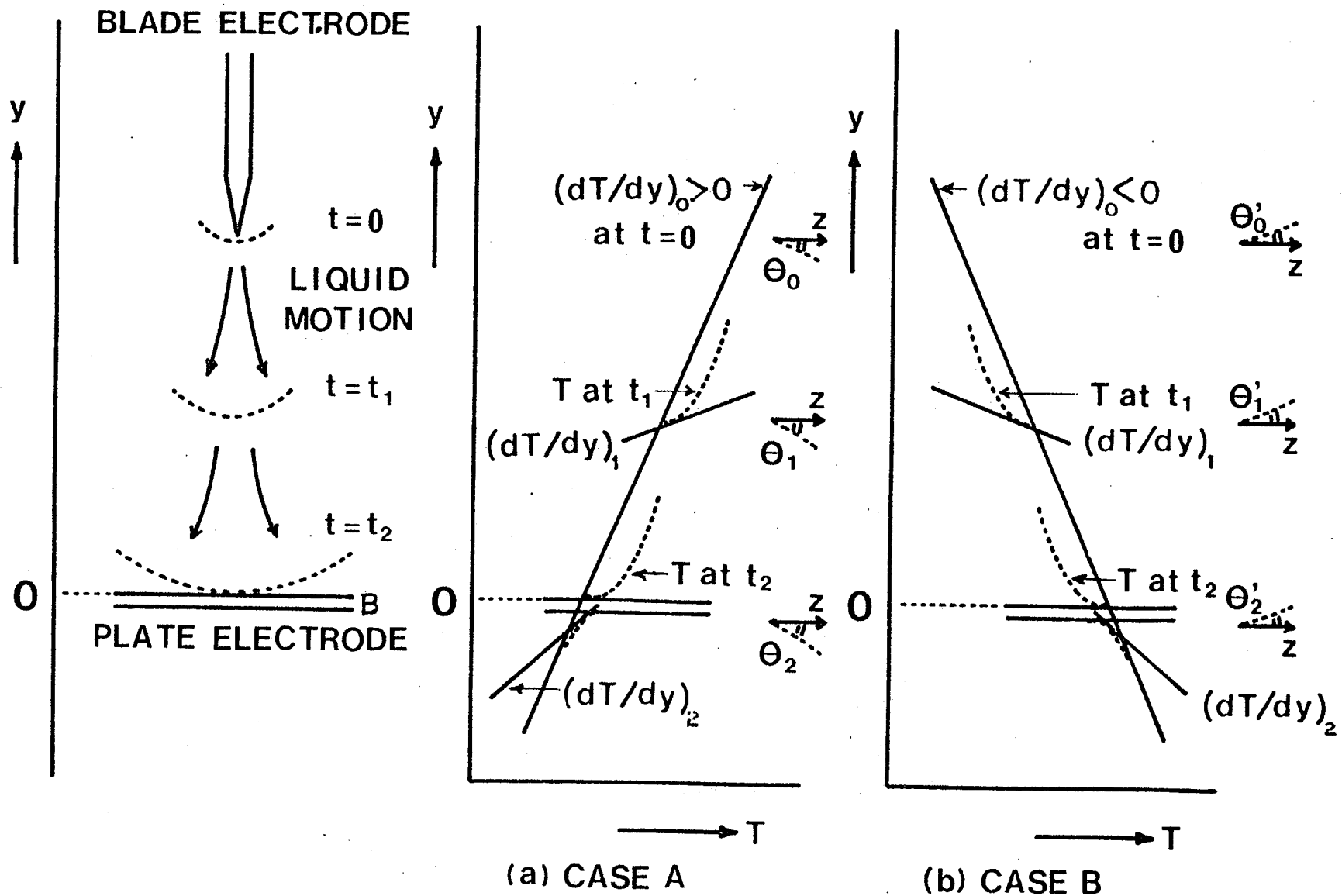
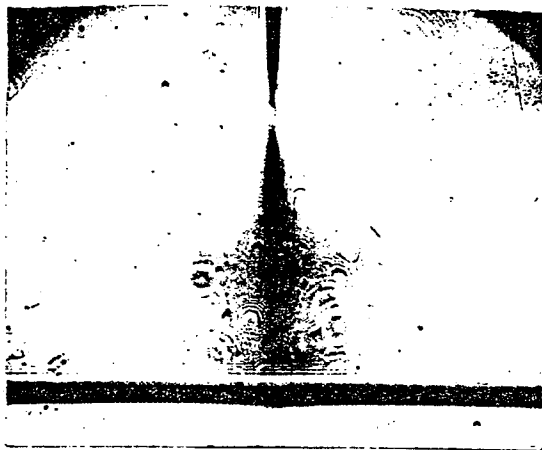


Fig. 4.2 Illustrating the change of the original temperature gradient at $t = 0$, $(dT/dy)_0$, resulting from the liquid motion caused predominantly by the motion of ions. (A) $(dT/dy)_0 > 0$ at $t = 0$; $(dT/dy)_1 > (dT/dy)_0$, $\theta_1 > \theta_0$; and $(dT/dy)_2$, $\theta_2 > \theta_0$; electromechanical force in the direction opposite to the ionic motion. (B) $(dT/dy)_0 < 0$ at $t = 0$; $(dT/dy)_1 < (dT/dy)_0$, $(2\pi - \theta'_1) < (2\pi - \theta'_0)$; and $(dT/dy)_2 < (dT/dy)_0$, $(2\pi - \theta'_2) < (2\pi - \theta'_0)$; electromechanical force in the same direction as the ionic motion.

initial $(dT/dy)_0 < 0$ shown in Fig. 4.2(b) than for the case with initial $(dT/dy)_0 > 0$ shown in Fig. 4.2(a).

Obviously, the situation described above and shown in Fig. 4.2 would be exhibited in Schlieren images. For case A corresponding to Fig. 4.2(a) the image brightness on the screen will decrease from the blade electrode towards the plate electrode while for case B corresponding to Fig. 4.2(b) this tendency will be just reversed if the knife edge is located as shown in Fig. 3.2. Thus from the Schlieren images we can determine which of the aforementioned mechanisms is dominant in causing the liquid motion provided that the temperature gradient in the liquid is known. Without sophisticated control of the temperature in the liquid, the spatial variation of temperature or the temperature gradient distribution in the liquid is quite random. Some typical Schlieren images for silicone oil at room temperature at an applied voltage of 7 kV across a blade-plate gap of 6 mm are shown in Fig. 4.3. It can be seen that with the knife edge located on the side shown in Fig. 3.2, the brightness of the Schlieren image for $(dT/dy)_0 > 0$ decreases with distance from the blade, and the dark region moves towards the plate as shown in Fig. 4.3(a). This tendency is just reversed for the case $(dT/dy)_0 < 0$ as shown in Fig. 4.3(b). It is important to note that the velocity of the dark region movement (or the bright region movement) towards the plate, though related to the liquid motion, does not give the actual velocity of the liquid motion, it merely shows the rate of the spatial variation of the refractive index in the test region. We also observed the following phenomena: (a) at the moment $(dT/dy)_0 = 0$, no Schlieren image was observed with the sensitivity of our Schlieren system,



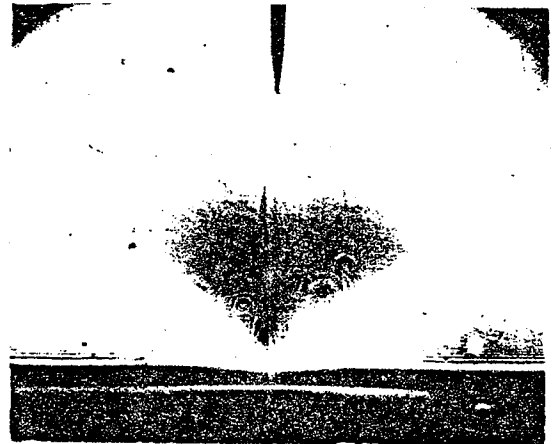
(a)



(d)



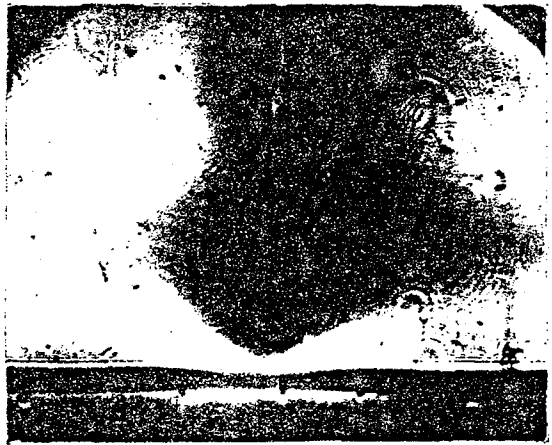
(b)



(e)



(c)



(f)

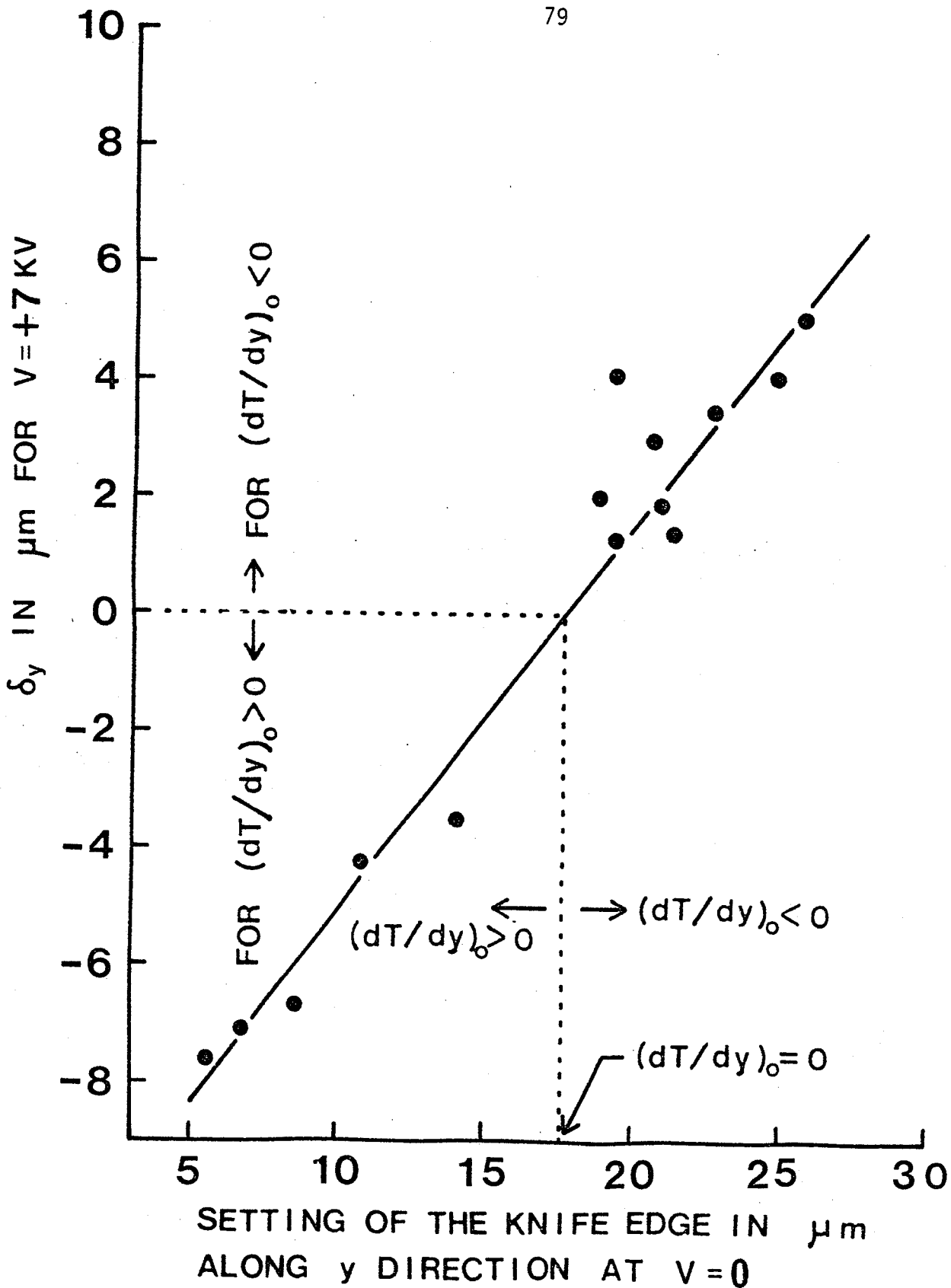
(A) $(dT/dy)_0 > 0$ (B) $(dT/dy)_0 < 0$

- g. 4.3 Schlieren photographs for silicone oil after the application of + 7 kV to the blade at $t = 0$ showing the effect of the already-existing temperature gradient in the test region. (A) $(dT/dy)_0 > 0$ corresponding to the knife edge setting of $5\mu\text{m}$; a, $t = 0.5$ sec; b, $t = 1.0$ sec; c, $t = 8.0$ sec; (B) $(dT/dy)_0 < 0$ corresponding to the knife edge setting of $30\mu\text{m}$.

and (b) the liquid motion in the y -direction was slowed down when $(dT/dy)_0 > 0$ and speeded up when $(dT/dy)_0 < 0$; as expected on the basis of the theory.

In the absence of applied voltages, we sometimes observed the Schlieren images, but the brightness of these images varied from time to time and from domain to domain indicating that the already-existing temperature gradients in the liquid varied from time to time and from domain to domain though the variation was small. However, with applied voltages and with a non-zero already-existing temperature gradient in the liquid, we always observed the Schlieren images. These images indicate that the liquid motion in silicone oil was always directed from the blade to the plate irrespective of the polarity of the applied voltage at the blade. It is obvious that if the blade injects electrons to form negatively charged ions or injects holes to form positively charged ions [Sueda and Kao 1979] then the liquid motion should always be directed from the blade to the plate. Even though the carrier injection is negligible at low fields, the presence of a high concentration of ionic impurities, such as in the case of silicone oil, would produce the liquid motion in the direction from the blade to the plate because the field is extremely high at the blade edge [Secker and Aplin 1970, Morant 1960]. The blade edge would easily neutralize the heterocharged ions and repulse the homo-charged one, thus creating a force directed from the blade to the plate. A similar liquid motion directed from the blade to the plate was also observed in water under a very low applied voltage. Yamashita et al. [1978] have reported that in transformer oil the liquid motion always starts at the needle point electrode and is directed towards the plane electrode.

Although in this investigation the temperature in the liquid was not controlled, we could always find an interval with a positive temperature gradient (the temperature increased from the plate to the blade), $(dT/dy)_0 > 0$, and an interval at some other time with $(dT/dy)_0 < 0$. By continuously monitoring the temperature variation in the liquid and patiently waiting for desired temperature gradients, we have performed a series of experiments about the change of the temperature gradients at point P_1 (0.7 mm above the plate) and at point P_2 (0.9 mm below the plate) due to the application of +7 kV or -7 kV to the blade electrode. With various initial temperature gradients $(dT/dy)_0$ prior to the application of the voltage ($V = 0$), we have measured δ_y at point P_1 corresponding to the change of the temperature gradient at time t after the application of a voltage to the blade, that is the quantity $(dT/dy)_t - (dT/dy)_0$. The measurements were made at $t = 0^-$ for $(dT/dy)_0$ with $V = 0$ and at $t = 2.5$ sec for $(dT/dy)_t$ after the application of +7 kV to the blade electrode at $t = 0^+$. The results are shown in Fig. 4.4. Similar results for -7 kV applied to the blade are shown in Fig. 4.5. These results show clearly that the movement of positive ions (or negative ions) from the blade to the plate will increase the temperature gradient towards the plate if the initial $(dT/dy)_0$ is positive, and decrease the temperature gradient towards the plate if the initial $(dT/dy)_0$ is negative, as illustrated in Fig. 4.2. It should be noted that, according to Equation (3.15), the deflecting distance δ_y of $1\mu\text{m}$, which is the distance of the knife-edge position from the original knife edge position at zero temperature gradient of $2.9 \times 10^{-3} \text{ K cm}^{-1}$ in the test cell for $f = 20 \text{ cm}$ $L = 5 \text{ cm}$ and $K_n = 3.4 \times 10^{-4} \text{ K}^{-1}$. The value of K_n was measured in our Material Laboratory at room temperature ($\sim 20^\circ\text{C}$).



g. 4.4 The temperature gradient in terms of δ_y measured at point P_1 (0.7 mm above the plate) after the application of + 7 kV to the blade as a function of the initial temperature gradient $(dT/dy)_0$ in terms of setting of the knife edge at zero applied voltage.

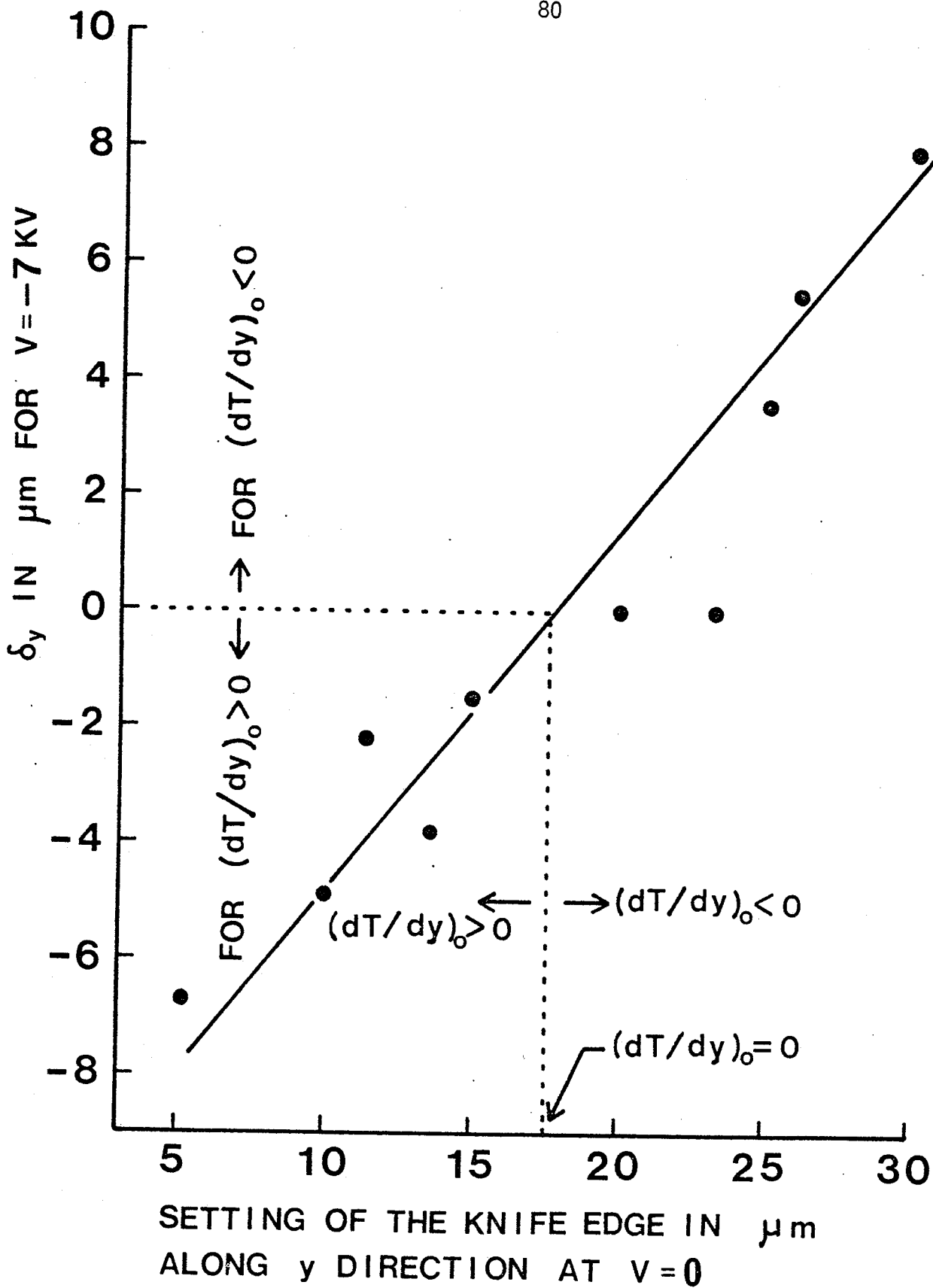


Fig. 4.5 The temperature gradient in terms of δ_y measured at point P_1 (0.7 mm above the plate) after the application of - 7 kV to the blade as a function of the initial temperature gradient $(dT/dy)_0$ in terms of setting of the knife edge at zero applied voltage.

We have also measured the transient change of the temperature gradient at point P_1 after the application of +7 kV (or -7 kV) to the blade electrode. The results are shown in Fig. 4.6. The curves for +7 kV and those for -7 kV at the blade are very similar. However, the liquid motion for case B (with $(dT/dy)_0 < 0$) was more rapid and more rigorous than that for case A (with $(dT/dy)_0 > 0$) as predicted from Fig. 4.2. The maximum change in δ_y and the time required for such a change to reach its maximum value depend on the initial temperature gradient $(dT/dy)_0$. In Table 4.1 are summarized the results of the maximum change in δ_y and the time required for such a change to reach its maximum value under various conditions. It should be noted that the knife edge setting corresponding to $(dT/dy)_0 = 0$ is $17.50\mu\text{m}$, and the settings smaller than $17.50\mu\text{m}$ correspond to $(dT/dy)_0 > 0$ and those greater than $17.50\mu\text{m}$ to $(dT/dy)_0 < 0$ as shown in Figs. 4.4 and 4.5. It can be seen in Table 4.1 that the larger the value of $|(dT/dy)_0|$, the greater is the maximum change in δ_y , and the shorter is the time required for this change to reach its maximum value. This time is obviously related to the time required for the unipolar ions to move from the blade electrode to point P_1 , and it is thus associated with the effective mobility of ions. This implies that the dependence of the ionic mobility on the already-existing temperature gradient $(dT/dy)_0$ is significant though $(dT/dy)_0$ is small because the latter modifies the liquid motion velocity. The importance of the already-existing temperature gradient to the measurements of ionic mobilities has not yet been realized although many investigators [Hewish 1979, Gray and Lewis 1969, 1965] have reported the effects of the liquid motion on the mobilities of ions. This observation suggests that to

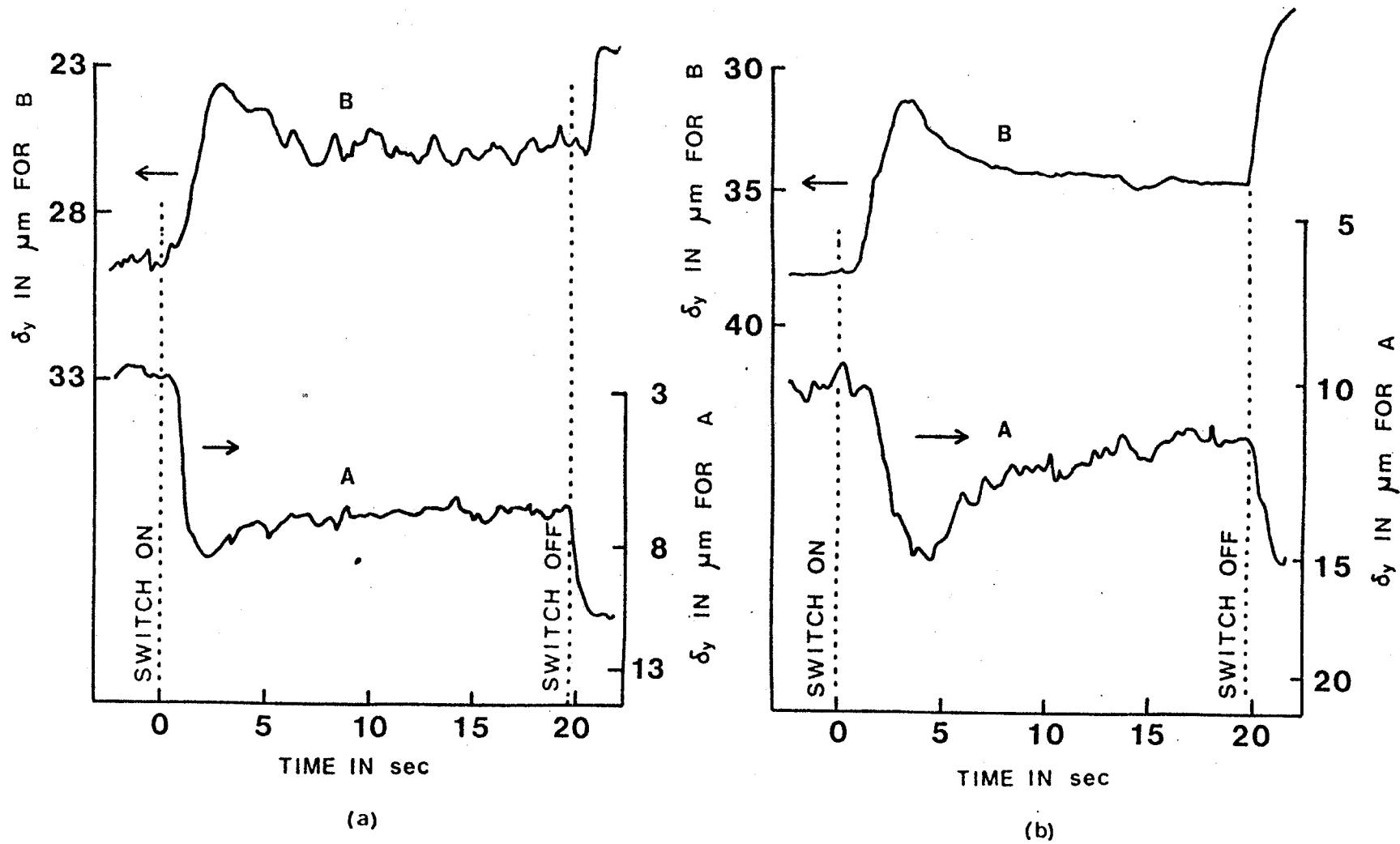


Fig. 4.6 The variation of δ_y with time measured at point P_1 (0.7 mm above the plate) after the application of 7 kV to the blade at $t = 0$ (switch on) and after the removal of the applied voltage at t of about 20 sec (switch off). (a) Applied voltage: + 7 kV; A: $(dT/dy)_0 > 0$ corresponding to the knife edge setting of $13.4\mu\text{m}$; B: $(dT/dy)_0 < 0$ corresponding to the knife edge setting of $25.5\mu\text{m}$; (b) Applied voltage: - 7 kV; A: $(dT/dy)_0 > 0$ corresponding to the knife edge setting of $10\mu\text{m}$; B: $(dT/dy)_0 < 0$ corresponding to the knife edge setting of $30\mu\text{m}$.

Table 4.1 The summary of the results about the relative maximum change in δ_y and the time t required for such a change to reach a peak value under various conditions.

Voltage at the Blade	+7 kV				-7 kV			
	$(dT/dy)_0 > 0$		$(dT/dy)_0 < 0$		$(dT/dy)_0 > 0$		$(dT/dy)_0 < 0$	
Knife edge setting, μm	13.40	-6.00	25.50	31.00	10.00	3.00	30.00	25.00
Relative value of $(dT/dy)_0$, μm	4.10	23.50	-8.00	-13.50	7.50	14.50	-12.50	-7.50
Maximum change in δ_y , μm	6.07	16.67	5.96	13.89	6.53	11.00	6.70	3.83
Time t , sec	2.19	2.19	2.94	1.54	4.56	3.88	3.44	4.38
Reference	Fig.4.6(a) Fig.4.7(A)	Fig.4.6(a) Fig.4.7(B)	Fig.4.6(b) Fig.4.8(A)	Fig.4.6(b) Fig.4.8(B)				

Knife edge setting of $17.50\mu\text{m}$ corresponds to $(dT/dy)_0 = 0$ based on the results shown in Figs. 4.4 and 4.5